A Stabilized High-Order Spectral Model with Adaptive Residual-based Artificial Viscosity for Fully-Nonlinear Free-Surface Flow

Longfei Cong*[1,2,3], Bin Teng[3], Wei Bai[4], and Zaijin You [2,5]

[1]Marine Engineering College, Dalian Maritime University, Dalian 116026, China

[2]Centre for Ports and Maritime Safety, Dalian Maritime University, Dalian 116026, China

[3]State Key Laboratory of Coastal and Offshore Engineering, Dalian University of Technology, Dalian 116024, China

[4]Department of Computing and Mathematics, Manchester Metropolitan University, Manchester M1 5GD, United Kingdom

[5]College of Transportation Engineering, Dalian Maritime University, Dalian 116026, China

Abstract

In the present work, a stabilized High-Order Spectral (HOS) model with adaptive residual-based artificial viscosity (RAV) has been developed for performance enhancement about fully-nonlinear free-surface flow simulation. To suppress the numerical instability caused by the nonlinear wave-wave interactions, i.e., the nonlinear mode-coupling between eigen-modes, with explicit time-domain integrator, additional estimations about the numerical residuals of free-surface elevation and free-surface potential with their backward histories have been carried out for stability-indicating and artificial viscous terms have been suggested to balance such unphysical energy-accumulation, especially for under-resolved wave components. Uppon the normalized free-surface residuals as the scales of artificial viscosity, even-order dissipation term has been assembled for energy-suppression. To remain the overall explicit algorithm, such additional dissipation has been considered in an operator-splitting manner. For the proposed dissipation algorithm, it has been shown that the present residual-based artificial energy-suppression holds the spectral-vanishing property because of its wave-number-related normalization in wave-number space. With such spectral normalization, the dissipation for the lower-wave-number well-resolved wave components has been well-controlled with the increase of dissipation order. Compared with the commonly-used spectral-filtering-based stabilization algorithm, where the energy-suppression within single-step free-surface prediction shows independency to the temporal increment (δt), the developed residual-based algorithm holds the solution-adaptive property, leading to an enhanced convergence performance of the free-surface model with its stabilization term tightly coupled to δt. To check the performance of the present RAV-HOS model, series of classical benchmarks, both numerical and experimental, have been reproduced, and a HOS-based Numerical-Wave-Tank (HOS-NWT) has been built as a preparation for our further investigations about wave-wave and wave-structure interactions. With the confirmation about both robustness and accuracy of the proposed stabilized HOS model, the promising prospect for its further application in oceanic, offshore and marine engineering as an efficient free-surface simulator has been expected.

Keywords: Free-Surface Flow; Fully-Nonlinear; High-Order Spectral Model; Numerical Residual; Stability-Indicator; Adaptive Artificial Viscosity; Numerical-Wave-Tank

*Corresponding author: conglongfei@dlmu.edu.cn

1 Introduction

During the past decades, the hydrodynamics of free-surface flows, e.g., gravity waves and liquid sloshing in oceanic, offshore and marine engineering, have attracted plenty of attentions from both engineers and scientists. Because of the rich flow-physics it contains, such a nontrivial task has been treated as a longstanding scientific problem for theoretical, experimental, and computational fluid dynamics (Engsig-Karup et al., 2016).

Along its history of development, the dimension-reduction models, which mainly include the shallow-water model (Vreugdenhil, 1994), Green-Naghdi model (Green and Naghdi, 1976) and Boussinesq model (Peregrine, 1967; Madsen et al., 1991), have been extremely popular, especially for shallow to medium water cases. With the increase of water-depth, the nonlinearity and dispersibility of free-surface flow lead to the necessity of the full-dimension potential-based nonlinear flow models for the balance between accuracy and efficiency (Tsai and Yue, 1996). Following the pioneering work by Longuet-Higgins and Cokelet (1976), the potential-based fully-nonlinear free-surface flow model has been well-developed (Grilli et al., 2001; Ferrant et al., 2003; Ning and Teng, 2007; Lin et al., 2021; Harris et al., 2022). Compared with the lower-order models, e.g., the Boundary Element model (BEM) (Teng and Eatock Taylor, 1995), Finite Volume model (FVM) (Lin et al., 2021) and Finite Element model (FEM) (Ma and Yan, 2006), spectral model has been well-developed in recent years because of its so-called spectral accuracy and the resulting numerical efficiency (Tian and Sato, 2008; Yates and Benoit, 2015; Raoult et al., 2019). Other than the high-order Finite Difference model (FDM) from Bingham and Zhang (2007) and Engsig-Karup et al. (2009), the vertical Chebyshev-fitting about the flow-potential improves the numerical performance of the Boundary-Value-Problem (BVP) solver considerably. Compared with the partial-spectral model, e.g., the vertical spectral model, as a full-spectral one, Dommermuth and Yue (1987) and Craig and Sulem (1993) have developed the High-Order Spectral (HOS) model with double Fourier-expansion to describe the free-surface elevation and to resolve the BVP about flow-potential by an eigen-expansion algorithm. With the help of Fast-Fourier-Transformation (FFT), quasi-linear complexibility has been achieved and such property leads to excellent efficiency of such free-surface model. As its extension to wave-structure interactions, Ducrozet et al. (2012) further assembled the wave-making algorithm to the HOS model and has built the HOS-based Numerical-Wave-Tank (HOS-NWT). Furthermore, for complicated cases with non-flat seabed in offshore engineering, Liu and Yue (1998), Guyenne and Nicholls (2008) and Gouin et al. (2016) developed the mode-coupling algorithm to resolve the fully-nonlinear free-surface flow and the arbitrary topography simultaneously. Different from the perturbation-based recursive algorithm to achieve the Dirichlet-to-Neumann (D2N) operator, with the separation of local and global nonlinear components in the projected Boundary-Integral-Equation (BIE), Clamond and Grue (2001) and Fructus et al. (2005) have also developed a spectral Boundary Element model to resolve the potential-related BIE in a spectral manner.

As it has been mentioned, with global eigen-expansion about the free-surface potential and free-surface elevation, spectral accuracy can be reached with HOS algorithm. Compared with the lower-order model (Ma and Yan, 2006; Lin et al., 2021), the global higher-order approximations about both free-surface elevation and free-surface potential lead to quite a low numerical dissipation. On the other hand, for Zakharov's equations (Zakharov, 1968), considerable energy for higher-wave-number wave components accumulates because of the nonlinear lower-order wave-wave interactions. With the explicit time-domain flow-predictor, higher-wave-number modes cannot be well-resolved because of the numerical stiffness and it leads to numerical issues to break the simulation without specified energy-suppression for such under-resolved wave components. Considering the complex higher-order nonlinearity and the iterative algorithm during D2N operation, an efficient implicit time-domain-integrator for HOS model is nontrivial to achieve due to the difficulty in Jacobi-evaluation for a rapid convergence during implicit nonlinear iterations, e.g., Newton-Raphson processes. As an alternative strategy, spectral-filtering has been commonly-used to filter out such undesirable higher-wave-number wave modes explicitly (Dommermuth and Yue, 1987; Guyenne and Nicholls, 2008). With such explicit filtering, the decoupling between temporal increment (δt) and filtering strength leads to a careful pre-determination about filtering parametres, which mainly include the filtering interval and energy-suppression rate. According to our numerical experiences, such a case-by-case parametre selection is nontrivial and a careless configuration will break the convergence and accuracy of the free-surface model. Compared with the spectral-filtering strategy, artificial viscosity has also been well-developed following VonNeumann and Richtmyer (1950) to control the shock-wave-related numerical oscillations for compressible fluid flows. With the explicitly-defined dissipation term, the growth of undesirable higher-wave-number modes has been suppressed to maintain the numerical performance of the model. Inspired by such a pioneering work, Spectral-Vanishing-Viscosity (SVV) (Tadmor, 1989; Karamanos and Karniadakis, 2000; Xu and Pasquetti, 2004) has been developed either as a stabilization scheme or to drive a Large Eddy Simulation (LES) about viscous fluid flow. Similar with the spectral-filtering approach, artificial viscosity has been dominantly-defined in the higher-wave-number region and the vanishing viscosity for well-resolved flow components maintains the numerical performance of the model (Hesthaven and Kirby, 2008; Engsig-Karup et al., 2016). Even spectral accuracy can be maintained with the mentioned dissipation model, there are still free parametres to be user-defined. To drive a solution-based dissipation, Guermond et al. (2011) and Dzanic and Witherden (2022) suggested the entropy-based stabilization strategy with entropy-residuals to measure the artificial viscosity adaptively. Recently, with the development of machine-learning, Schwander et al. (2021) and Coutinho et al. (2023) have further achieved the neural-network-based determination about the viscosity scale. Similar with the entropy-based model, with the numerical residuals of conservation laws as the discontinuity- (or instability-) indicator, residual-based artificial viscosity has been raised as an alternative strategy to control the shock-wave-induced numerical oscillation (Nazarov and Hoffman, 2013; Stiernstrom et al., 2021; Dao and Nazarov, 2022; Tominec and Nazarov, 2022). Without the selection of entropy pair, together with truncation wave-number and viscosity scale, the robustness and accuracy of such solution-adaptive artificial viscosity strategy has been shown to be satisfactory (Nazarov and Hoffman, 2013; Tominec and Nazarov, 2022).

Generally speaking, compared with the well-developed artificial viscosity approach for stable numerical simulation about conservation laws, its extension to potential-based free-surface flow simulation has not been addressed to the best of our knowledge. As it has been mentioned, such a combination meets difficulties in at least two aspects:

(1) For conservation laws, the numerical instability relates to the strong flow discontinuity, i.e., the shock wave, which is obvious a local flow behaviour, leading to the locally-defined artificial viscosity. While, within the potential-based free-surface model, the incompressible fluid flow is always smooth (except the local singularities around geometrical-unsmooth domain corners). Therefore, it is believed that the main source of the numerical instability is the nonlinear mode-coupling between lower-order wave components. In this way, rather than its shock-wave-related local definition in physical space for conservation laws, the proposed artificial viscosity for potential flow should be globally designed to suppress the undesirable energy accumulation and the relating numerical instability within higher-wave-number region.

(2) To avoid the scaling effect, or in other words, to make the free model-parametres dimensionless, the artificial viscosity should be scaled with some explicitly-defined flow variables. For conservation-law-simulation with residual-based artificial viscosity, the numerical residual has been normalized with local equal-dimension parametres, which relate to both their maximum and minimum values around neighboring elements and acts as the discontinuity-indicator. For the potential flow, because of its mode-by-mode definition about the artificial viscosity, such normalization should also be considered in a different way to meet the global property of stability-indicator. On the other hand, within the previous artificial-viscosity-based stabilization for conservation laws, the dissipation order has always been defined as $p = 1$ for its consistency with physical viscous effect. While, for potential-based free-surface model, higher-order coupling up to 4_{th} order exists in Zakharov's equations. Therefore, the dissipation order selection and its effect on model performance should also be considered and confirmed with care.

As it has been discussed, considering both its efficiency and accuracy in free-surface potential-flow-simulation, in the present work, an improved fully-nonlinear HOS-based free-surface model with residual-based artificial viscosity (RAV) for an enhanced numerical stability has been developed. To suppress the undesirable wave-energy within under-resolved wave-region caused by lower-order mode-coupling, a residual-based dissipation strategy has been raised. Within the proposed stabilized HOS framework, explicit predictions about free-surface elevation and free-surface potential have been carried out with an explicit Runge-Kutta (RK) scheme. During each sub-stage of the explicit time-domain-RK-integrator, estimations about the free-surface numerical residuals have been carried out for stability-indicating and further to measure the artificial viscous coefficients. With the introduction of an even-order dissipation term, the solution-based artificial viscosity has been normalized in wave-number space with the corresponding modal-amplitudes of free-surface potential and free-surface elevation mode-by-mode. Within such energy-suppression model, spectral-vanishing property has been produced with the increase of dissipation order p, and its solution-based adaptive property leads to a convenient stabilization algorithm free from user-defined wave-number-truncation and dissipation strength determination. With the numerical experiments about various of benchmarks, it has been shown that the convergence performance of the proposed RAV-HOS model has been enhanced considerably, compared with the spectral-filtering-based ones, and the numerical accuracy of the model has also been maintained. Furthermore, with the developed RAV-HOS model as the flow solver, Numerical-Wave-Tank (NWT) has been built for both regular and irregular wave generation. With the preliminary simulation about regular waves, irregular focus waves and pressure-driven ship-waves, it shows the feasibility for the application of the present RAV-HOS-NWT model to our future research topics for both wave-dynamics and wave-structure interactions.

In the remaining parts, the present research has been organized as following: In Sec. 2, the principle of the incompressible ideal fluid dynamics, including both the governing equations and corresponding boundary conditions, will be discussed briefly; In Sec. 3, the basic numerical algorithms for the HOS model to resolve the potential-related BVP, together with the residual-based adaptive stabilization strategy for higher-wave-number energy-suppression, will be introduced; In Sec. 4, numerical simulation about classical benchmarks will be carried out to check the performance of the proposed numerical model and the RAV-HOS-based Numerical-Wave-Tank (RAV-HOS-NWT) will be built for wave simulation; Lastly, in Sec. 5, the main findings and conclusions of the present work will be summarized.

2 Governing Equations

Presently, the fluid domain is bounded by the side-wall (not shown for briefness), the free-surface and the seabed, as shown in Fig. 1. To describe the geometry and the fluid flow, a Cartesian coordinate system $o-xyz$ has been built with z axis pointing upward and $z=0$ on the still water-level. With the single-value assumption about the free-surface elevation, which is available for gravity waves and liquid sloshing without violent deformation, the interface between fluid and atmosphere has been defined as $z=\eta(x,y,t)$, where t denotes the time. At the same time, with identical assumption about the seabed as a material surface, such stationary boundary has been defined as $z=-h(x,y)$. With the neglection about both viscosity and compressibility of the fluid flow, its motion free from initial vorticity can be described by a flow-potential ϕ, and the flow velocity can be defined as $u=\nabla\phi=(\nabla_h\phi,\frac{\partial\phi}{\partial z})$, where $\nabla=(\nabla_h,\frac{\partial}{\partial z})=(\frac{\partial}{\partial x},\frac{\partial}{\partial y},\frac{\partial}{\partial z})$ denotes the 3D gradient operator, and $\nabla_h=(\frac{\partial}{\partial x},\frac{\partial}{\partial y})$ denotes its horizontal component. On the seabed, the no-penetration condition should be satisfied and it has been modelled as a normal-flux-vanishing Boundary-Condition (BC) $\phi_n=0$. In the present work, only flat seabed has been considered, leading to $\phi_n=\phi_z=0$ on the bottom of the fluid domain. On the free-surface $z=\eta$, the motion of fluid particle along tangential direction of the free-surface, together with the pressure balance between fluid flow and atmosphere, leads to the following BCs

$$\frac{\partial\eta}{\partial t}+\nabla_h\eta\cdot\nabla_h\phi=\phi_z, \tag{1}$$

$$\frac{\partial\phi}{\partial t}+\frac{\nabla\phi\cdot\nabla\phi}{2}+g\eta=0. \tag{2}$$

With Zakharov's definition about the free-surface potential $\phi_s(x,y)=\phi(x,y,z=\eta(x,y))$ (Zakharov, 1968), evolution equations for free-surface elevation and free-surface potential can be reformulated from Eqs. (1) and (2) as

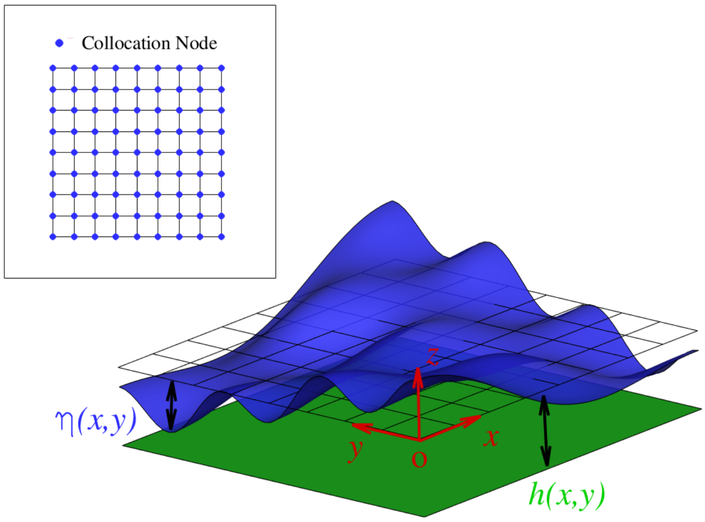

Fig. 1. Sketch diagram of the fluid domain, together with the collocation grid setting.

$$\frac{\partial \eta}{\partial t} = (1 + \nabla_h \eta \cdot \nabla_h \eta)\phi_z - \nabla_h \phi_s \cdot \nabla_h \eta, \tag{3}$$

$$\frac{\partial \phi_s}{\partial t} = -g\eta - \frac{\nabla_h \phi_s \cdot \nabla_h \phi_s}{2} + \frac{1 + \nabla_h \eta \cdot \nabla_h \eta}{2}(\frac{\partial \phi}{\partial z})^2. \tag{4}$$

It can be obviously observed from Eqs.(3) and (4) that, with the well-defined ϕ_s and η at certain temporal stage, their future states can be predicted by the time-domain-integration, with the determination of $\phi_z|_{z=\eta} = w|_{z=\eta}$, i.e., the vertical flow velocity on the free-surface. For such D2N operation ($\phi_s \to \phi_z|_{z=\eta}$), considering the well-defined $\eta(x, y)$ at certain time, the fluid domain can be defined as $\Omega = (x, y, -h(x, y) \leq z \leq \eta(x, y))$. Meanwhile, the free-surface potential ϕ_s has also been obtained by time-domain integration. Therefore, a closed-form Boundary-Value-Problem (BVP) follows

$$\nabla^2 \phi = 0, \tag{5}$$

with the boundary condition

$$\begin{aligned} \phi &= \phi_s, \quad at \quad z = \eta, \\ \phi_n &= 0, \quad at \quad z = -h. \end{aligned} \tag{6}$$

On the lateral boundaries, which have been assumed as vertical side-walls in the present research, Neumann-type boundary condition can be defined for the boundary flux ϕ_n, which is the case for free-surface flow within a closed container. In the present work, $\phi_n = 0$ has been adopted to drive the double Fourier-expansion.

As it has been observed, the key component to drive the evolution of ϕ_s and η is the determination of $\phi_z|_{z=\eta}$. To obtain such values, the BVP defined by Eq. (5) and boundary conditions Eq. (6) should be resolved. As it has been discussed in Sec. 1, various approaches, e.g., BEM, FEM and FVM, can be adopted as the flow-potential solver. For the fully-nonlinear free-surface flow, all the mentioned schemes share the so-called Mixed-Euler-Lagrange or Semi-Euler-Lagrange approach to predict the changeable free-surface. To obtain a solution domain with unchanged geometry for the purpose of simplification on the overall algorithm and to improve the numerical performance of the model, perturbation approach has been adopted in the present work to map the free-surface potential to its mean location, i.e., $z = 0$. To drive such perturbation-based BVP-resolving algorithm, assumption has been made about the free-surface elevation, i.e., $\eta = O(\epsilon)$, considering the fact that the wave-steepness $\epsilon = kA$ is small. Furthermore, for the fluid flow driven by the $O(\epsilon)$ free-surface elevation, identical assumption can be made about the free-surface potential, i.e., $\phi_s = O(\epsilon)$. With $O(\epsilon)$ assumption about both free-surface elevation and free-surface potential, the detailed iterative algorithm to resolve the BVP (Eqs. (5) and (6)) will be described in the following section, together with the residual-based artificial dissipation strategy for performance enhancement about the time-domain integrator.

3 Numerical Methods

In this section, the numerical algorithms for the proposed HOS-based free-surface model will be discussed. As it has been mentioned in Sec. 1, to suppress the undesirable energy accumulation because of the nonlinear mode-coupling for higher-wave-number wave components, the residual-based artificial viscosity has been raised for stability enhancement and the relating performance analysis will also be carried out in detail.

3.1 High-Order Spectral (HOS) Method

As it has been discussed in Sec.2, the D2N operator, which relates to the resolving of a potential-related BVP, should be achieved in an efficient manner to drive the evolution of free-surface. Unlike the linear case, where all the linearized BCs are defined on the mean free-surface and the matrix-reversion operation can be done once only for efficiency enhancement, for the nonlinear case, the relating linear-algebra should be re-defined to match the varying free-surface. For the spectral model, even eigen-expansion algorithm, as it has been developed in Fenton (1988) and Ferrant and Le Touzé (2001), can be adopted to resolve the modal coefficients by matching the free-surface BC (Eq. (6)) in a collocation manner, the iterative dense-matrix re-assembling and reversion operation limit the efficiency of the fully-nonlinear free-surface simulation.

In the HOS framework, eigen-expansion has also been executed to resolve the BVP with spectral accuracy, as it has been done by Ferrant and Le Touzé (2001). To match the instantaneous free-surface to its mean status for domain-regulation, perturbation expansion has also been carried out. Assuming the flow-potential is in the form $\phi = \Sigma_m \phi^{(m)}$, where $\phi^{(m)} = O(\epsilon^m)$, the flow-potential on the free-surface, i.e., the free-surface potential ϕ_s, can be obtained by its Taylor-expansion about $z = 0$ as $\phi_s = \phi + \frac{1}{1!}\frac{\partial \phi}{\partial z}\eta + \frac{1}{2!}\frac{\partial^2 \phi}{\partial z^2}\eta^2 + ...$, where the RHS terms are all evaluated on $z = 0$. With a further assumption $\eta = O(\epsilon)$, such expansion can be further rewritten as

$$\begin{aligned}\phi_s = \quad & \phi^{(1)} \\ & + \frac{1}{1!}\frac{\partial \phi^{(1)}}{\partial z}\eta + \phi^{(2)} \\ & + \frac{1}{2!}\frac{\partial^2 \phi^{(1)}}{\partial z^2}\eta^2 + \frac{1}{1!}\frac{\partial \phi^{(2)}}{\partial z}\eta + \phi^{(3)} + \ldots.\end{aligned} \tag{7}$$

It has been mentioned in Sec.2 that $\phi_s = O(\epsilon)$. Therefore, the mean-free-surface potential can be obtained by the order-clustering algorithm about ϵ and the recursive BVP can be defined order-by-order. For a certain l_{th} order BVP, it follows

$$\nabla^2 \phi^{(l)} = 0, \tag{8}$$

with the boundary condition

$$
\begin{aligned}
&\phi^{(l)} = \phi^{(l)}_{mean}, \quad at \quad z = 0, \\
&\phi^{(l)}_n = 0, \quad at \quad z = -h.
\end{aligned} \tag{9}
$$

For the fluid flow within a closed container, i.e., $x_0 \le x \le x_0 + L_x$ and $y_0 \le y \le y_0 + L_y$, such flow potential can be expanded with eigen-functions as

$$
\phi^{(l)} = \Sigma_{m,n} A^{(l)}_{m,n}(z) cos[k_m(x - x_0)] cos[k_n(y - y_0)]. \tag{10}
$$

To satisfy Eq.(8), the modal-amplitude $A^{(l)}_{m,n}(z)$ should follow

$$
A^{(l)}_{m,n}(z) = \begin{cases} C^{(l)}_{1,0,0} + C^{(l)}_{2,0,0} z & m = 0 \quad and \quad n = 0 \\ C^{(l)}_{1,m,n} e^{k_{m,n} z} + C^{(l)}_{2,m,n} e^{-k_{m,n}(z+d)} & otherwise \end{cases}, \tag{11}
$$

where the factor $e^{-k_{m,n} d}$ has been introduced to avoid the numerical blowing up of exponential function and $k_{m,n} = \sqrt{k_m^2 + k_n^2}$, with $k_m = \frac{m\pi}{L_x}$ and $k_n = \frac{n\pi}{L_y}$ the horizontal eigen-values of the BVP with Neumann-type homogeneous BCs on the side-walls. To match BCs shown as Eq.(9), Galerkin approach has been adopted, considering the orthogonality between Fourier components. With cosine-transformation to Eq.(9), it can be obtained that

$$
FFT_{COS}(\phi^{(l)}_{mean})_{m,n} = \begin{cases} C^{(l)}_{1,0,0} & m = 0 \quad and \quad n = 0 \\ C^{(l)}_{1,m,n} + C^{(l)}_{2,m,n} e^{-k_{m,n} d} & otherwise \end{cases}, \tag{12}
$$

and

$$
0 = \begin{cases} C^{(l)}_{2,0,0} & m = 0 \quad and \quad n = 0 \\ C^{(l)}_{1,m,n} k_{m,n} e^{-k_{m,n} d} - C^{(l)}_{2,m,n} k_{m,n} & otherwise \end{cases}. \tag{13}
$$

It should be noted that, the present vertical-eigen-functions have been defined as the normal exponential function for its extention to non-flat seabed and multi-layer-fluid cases and it is equivalent to the $cosh(k_{m,n}z)$ and $sinh(k_{m,n}z)$ pair. To achieve an efficient cosine-type transformation, FFT routine provided by FFTW library (Frigo and Johnson, 2005) has been used to reach quasi-linear complexibility. With the well-resolved BVP, the D2N operator can be achieved as

$$
\begin{aligned}
\frac{\partial \phi}{\partial z}|_{z=\eta} = \; & \frac{\partial \phi^{(1)}}{\partial z} \\
& + \frac{1}{1!} \frac{\partial^2 \phi^{(1)}}{\partial z^2} \eta + \frac{\partial \phi^{(2)}}{\partial z} \\
& + \frac{1}{2!} \frac{\partial^3 \phi^{(1)}}{\partial z^3} \eta^2 + \frac{1}{1!} \frac{\partial^2 \phi^{(2)}}{\partial z^2} \eta + \frac{\partial \phi^{(3)}}{\partial z} + ...
\end{aligned} \tag{14}
$$

With such vertical velocity on the free-surface, the evolution equations Eqs.(3) and (4) can be integrated in the time-domain. In the present work, explicit TVD-RK3 scheme (Shu and Osher, 1988) has been adopted for an improved numerical performance and such scheme consists three sub-stages

$$
\begin{aligned}
&\Psi^{(0)} = \Psi^{(n)}, \quad \Psi^{(1)} = \Psi^{(0)} + \frac{\partial \Psi^{(0)}}{\partial t} \delta t, \\
&\Psi^{(2)} = \frac{3}{4} \Psi^{(0)} + \frac{1}{4} (\Psi^{(1)} + \frac{\partial \Psi^{(1)}}{\partial t} \delta t), \\
&\Psi^{(3)} = \frac{1}{3} \Psi^{(0)} + \frac{2}{3} (\Psi^{(2)} + \frac{\partial \Psi^{(2)}}{\partial t} \delta t), \\
&\Psi^{(n+1)} = \Psi^{(3)},
\end{aligned} \tag{15}
$$

where $\Psi^{(n)}$ represents either the free-surface elevation or the free-surface potential at $t = t^n$, and δt denotes the temporal increment. Furthermore, to evaluate the horizontal derivation terms in Eqs.(3) and (4), their physical values have been mapped to the modal-amplitudes in the wave-number space firstly, followed by the horizontal derivative operations, and then mapped back to the physical space. For the nonlinear terms in Eqs. (3) and (4), recursive $\frac{2}{3}$ rules have been used for dealiasing, if necessary.

3.2 Residual-based Artificial Viscosity Model

For linearized free-surface flow, Eqs.(3) and (4) can be reduced to $\frac{\partial \eta}{\partial t} = \phi_z$ and $\frac{\partial \phi_s}{\partial t} = -g\eta$. It is obvious that there are no mode-couplings with such linearization. In this case, the under-resolved wave components only come from their initial values and have no coupling with lower-wave-number well-resolved ones. Therefore, stability issue is not that obvious because of the lack of initial energy within the higher-wave-number region. While, for the fully-nonlinear cases, interactions between lower-wave-number components occur as the source of sum-wave-number components. With the accumulation for such higher-wave-number energy, numerical instability occurs. As it has been shown in Dommermuth and Yue (1987), spectral-filtering is an effective way to remove such numerical instability by filtering out the unstable higher-wave-number modes explicitly. Within such stabilized algorithm, the highest-wave-number component has been suppressed to 0 with the remaining components filtered by $\tilde{\psi}_{m,n} = \tilde{\psi}^{*}_{m,n}\Lambda(k_m)\Lambda(k_n)$ in wave-number space with

$$\Lambda(k) = \frac{1}{8}[5 + 4cos(\frac{\pi k}{k_{max}}) - cos(\frac{2\pi k}{k_{max}})], \tag{16}$$

or its simple extention $\tilde{\psi}_{m,n} = \tilde{\psi}^{*}_{m,n}\hat{\Lambda}(k_m)\hat{\Lambda}(k_n)$ with

$$\hat{\Lambda}(k) = 1 - (1 - \alpha_s)(1 - \Lambda(k)), \tag{17}$$

where the free parametre α_s has been adopted for dissipation controlling. Furthermore, within the spectral element framework from Engsig-Karup et al. (2016), an enhanced exponential filter (Hesthaven and Kirby, 2008) has been developed with similar free parametre to control the numerical dissipation for highest-wave-number component. Beyond the goal of present research, such topic will not be discussed further in detail. For the spectral-filtering strategy, free parametres exist and need to be pre-defined. With the well-selected parametres, they are kept as fixed values during the entire simulation. With the temporal duration for free-surface flow prediction fixed as ΔT, it is assumed that no external excitation (free-surface pressure or free-surface mass source/sink) exists and the filtering operation has been executed at the end of each single-step explicit Euler prediction $t = n\delta t$. Denoting the mapping operator between ($\eta^{(n)}$, $\phi_s^{(n)}$) and ($\eta^{(n+1)}$, $\phi_s^{(n+1)}$) as $\mathscr{T}$, then the final state of the free-surface flow at $t = \Delta T$ can be obtained as ($\eta^{\Delta T}$, $\phi_s^{\Delta T}$) $= (\mathscr{D} \cdot \mathscr{T})^{\frac{\Delta T}{\delta t}} \cdot (\eta^0$, $\phi_s^0)$, with $\mathscr{D}$ the filtering operator. Considering that the filtering operator can be splitted into $\mathscr{D} = \mathscr{F}^{-1}\Lambda\mathscr{F}$, i.e., a forward Fourier transformation followed by a diagonal wave-number-space filtering and a backward Fourier transformation, for linear cases, the order of $\mathscr{D}$ and $\mathscr{T}$ can be exchanged because of the splitting $\mathscr{T} = I + \delta t\mathscr{F}^{-1}\Delta\tilde{\mathscr{T}}\mathscr{F}$, where $\Delta\tilde{\mathscr{T}}$ denotes the block anti-diagonal matrix consisting of identical mapping and the wave-number-space diagonal D2N operators, as shown in Eqs. (3) and (4). In this situation, the mentioned free-surface prediction can be rewritten as ($\eta^{\Delta T}$, $\phi_s^{\Delta T}$) $= \mathscr{T}^{\frac{\Delta T}{\delta t}} \cdot [\mathscr{D}^{\frac{\Delta T}{\delta t}} \cdot (\eta^0$, $\phi_s^0)]$, i.e., the unfiltered one with $[\mathscr{D}^{\frac{\Delta T}{\delta t}} \cdot (\eta^0$, $\phi_s^0)]$ as the 'filtered' initial condition. With the decrease of δt, $\frac{\Delta T}{\delta t}$ increases. It is obvious that the 'filtered' initial wave components will be dampened to zero except the spacial uniform one with the filters Eqs. (16) and (17). With such 'filtered' initial wave elevation and free-surface potential, the free-surface prediction will be obviously over-dissipative. For nonlinear cases, although the exchanging of $\mathscr{D}$ and $\mathscr{T}$ cannot be executed, similar phenomenon can be also expected with the increase of filtering iterations. As it will be shown in the next section, unsuitable parametres lead to convergence issues with $\delta t \to 0$. To launch the simulation, such pre-parametre-selection is obvious a nontrivial task.

As another effective strategy to provide energy-suppression for higher-wave-number flow components, artificial viscosity has been widely adopted to remove the shock-wave related numerical oscillation for conservation laws as it has been mentioned in Sec. 1. Inspired by VonNeumann and Richtmyer (1950), Tadmor (1989) and Guermond et al. (2011), in the present work, viscous terms have been assembled to Eqs. (3) and (4) to provide wave-number-related dissipation. Consistent with the previous ones, such term is in the form of $(\nu_x \otimes \frac{\partial^{2p}\Psi}{\partial x^{2p}} + \nu_y \otimes \frac{\partial^{2p}\Psi}{\partial y^{2p}})$, where $\otimes$ denotes the convolution operator, and in the wave-number space, it takes the normal '$\times$' form. In the present artificial dissipation model, free parametre p exists to achieve controlling about 'dissipation region' and further for the spectral-vanishing property of the energy-suppression model. With the increase of p, narrower filtering-higher-wave-number region can be obtained and the dissipation for the well-resolved wave components tends to 0. To achieve dimension-balancing, it is obvious that the viscosity parametres ν_x and ν_y are in the dimension of $\frac{L^{2p}}{T}$. As a natural choice, the length part for such balancing can be selected as δx^{2p} and δy^{2p} respectively. In this way, with the increase of model resolution, the dissipation will be weakened simultaneously. As it will be shown later, such dimension can also be selected as $\frac{1}{k^{2p}_{x,max}}$ and $\frac{1}{k^{2p}_{y,max}}$ for a consistent dissipation. Furthermore, the remaining time-scale will be selected as δt, and it has been merged to the definition about numerical residuals of Eqs. (3) and (4). It should be mentioned that, even with the decrease of δt, inconsistency seems to exist because of the $\frac{1}{\delta t}$ term in the viscosity definition, as it will be discussed later, the higher-order property of the residual term with respect to the temporal increment leads to the reproduction of vanishing viscosity with $\delta t \to 0$.

For the purpose to remove the priori determination about the dissipation strength, it is essential to achieve an adaptive algorithm to control the rate of energy-suppression, without breaking the accuracy of the original model, if possible. For HOS model, the relative 'large' temporal increment for higher-wave-number wave components leads to the stability issue, compared with the resolution-related mechanism about the shock-wave-related discontinuity for conservation laws. Considering such observation, a suitable stability-indicator is the key component to drive the artificial viscosity determination. In the present algorithm, the numerical residuals of Eqs.(3) and (4) are selected for such stability-indicating. For the general model equation $\frac{\partial \Psi}{\partial t} = R(\Psi, t)$, TVD-RK3 algorithm, i.e., Eq.(15), can be adopted as the time-domain integrator to obtain its explicit prediction Ψ^* with a local $O(\delta t^4)$ error. With a multi-step backward formula to evaluate the $\frac{\partial}{\partial t}$ term, such an explicit prediction leads to a numerical residual

$$D^{\partial t}(\Psi^*, \Psi^{(n)}, \Psi^{(n-1)}, ...) = R(\Psi^*, t^{n+1}) + Res, \tag{18}$$

where the backward temporal derivation $D^{\partial t}(\cdot)$ can be built with a polynomial-fitting algorithm in the time-domain. In the present research, considering the fact that only the local error for the final Ψ^* can be estimated as $O(\delta t^4)$, while the errors for its auxiliary predictions during the sub-integrator are only $O(\delta t^2)$ for a conservative estimation, only backward Euler scheme, i.e., the single-step BDF formula, has been adopted, that is

$$D^{\partial t}(\Psi^*, \Psi^{(n)}, \Psi^{(n-1)}, ...) = \frac{\Psi^* - \Psi^{(n)}}{\delta t}. \tag{19}$$

It is obvious that the implicit scheme is unconditional stable mostly. For the 'true' solution of such implicit formula, it can be obtained that

$$D^{\partial t}(\Psi^{implicit}, \Psi^{(n)}, \Psi^{(n-1)}, ...) = R(\Psi^{implicit}, t^{n+1}). \tag{20}$$

From Eqs. (18) and (20), the numerical residual follows

$$\begin{aligned} Res =& \frac{\alpha}{\delta t}(\Psi^* - \Psi^{implicit}) + R(\Psi^{implicit}, t^{n+1}) - R(\Psi^*, t^{n+1}) \\ =& (\frac{\alpha}{\delta t} - \frac{\partial R}{\partial \Psi^*})(\Psi^* - \Psi^{implicit}) \\ =& (\alpha - \frac{\partial R}{\partial \Psi^*}\delta t)\frac{\Psi^* - \Psi^{implicit}}{\delta t}. \end{aligned} \tag{21}$$

Considering the numerical accuracy of Eq. (20), compared with Eq. (15), $\Psi^* - \Psi^{implicit} = O(\delta t^h)$ with $h \geq 2$ holds and it leads to the linearization in Eq.(21). For an explicit time-domain integrator, its conditional stability for the lower-wave-number well-resolved wave components leads to $(\alpha - \frac{\partial R}{\partial \Psi^*}\delta t) = O(1)$. Therefore, within the well-resolved wave-number region, such numerical residual is $O(\delta t^{h-1})$, while with the increase of wave-number, the numerical stiffness leads to the failure of such estimation. With Res as the stability-indicator, the viscous coefficients $\nu_{x,y}$ can be well-scaled. Within the numerical residual defined in Eq. (18), time-scale exists naturally. Therefore, for dimension-balancing, such residual should be further normalized with a Ψ-scaled variable. As it has been shown in the appendix, $|\Psi|$ itself is a reasonable choice. In wave-number space, to avoid numerical blowing up, such normalization factor has been reformulated as $(\left|\tilde{\Psi}\right| + \left|\tilde{R}\right| \delta t + \epsilon)$, with $\epsilon = 10^{-8}$. According to the mentioned discussion, with a consistent nondimensional factor β for both ν_x and ν_y, the dissipation term can be written as

$$D(\Psi) = \beta \hat{Res} \otimes (\frac{1}{{k_{x,max}}^{2p}}\frac{\partial^{2p}\Psi}{\partial x^{2p}} + \frac{1}{{k_{y,max}}^{2p}}\frac{\partial^{2p}\Psi}{\partial y^{2p}}), \tag{22}$$

with $k_{x,max}$ and $k_{y,max}$ the wave-number bounds for $\frac{2}{3}$ dealiasing or dealiasing-free rule. Within the wave-number space, it can be formulated as

$$\begin{aligned} \tilde{D}(\Psi)_{m,n} &= \beta((\frac{k_m}{k_{x,max}})^{2p} + (\frac{k_n}{k_{y,max}})^{2p}) \times \frac{\tilde{Res}_{m,n}}{(\left|\tilde{\Psi}_{m,n}\right| + \left|\tilde{R}_{m,n}\right| \delta t + \epsilon)} \times \tilde{\Psi}_{m,n} \\ &= \beta[\sigma(\frac{k_m}{k_{x,max}}) + \sigma(\frac{k_n}{k_{y,max}})] \times \frac{\tilde{Res}_{m,n}}{(\left|\tilde{\Psi}_{m,n}\right| + \left|\tilde{R}_{m,n}\right| \delta t + \epsilon)} \times \tilde{\Psi}_{m,n}, \end{aligned} \tag{23}$$

with $\sigma(\cdot)$ acts as the spectral filter for the artificial viscosity. In the present work, to make such term always dissipative, $\left|\tilde{Res}_{m,n}\right|$ has been used instead of $\tilde{Res}_{m,n}$.

As it can be observed from Eq. (23), the artificial dissipation term in the wave-number-space can be splitted into the residual component and the filter component relating to dissipation order p. To show the effect of such dissipation order on the performance of RAV algorithm, Fig. 2 shows the strength of spectral filter with different ps and its comparison with the enhanced exponential filter proposed by Hesthaven and Kirby (2008). It can be observed from Fig. 2 that, with the normalized wave-number, dissipation within the lower-wave-number region can be suppressed to an arbitrary small value with the increase of p because of the vanishing of σ. In this case, the lower-wave-number wave components can be kept unfiltered and only the higher-wave-number ones are suppressed to keep the numerical stability, leading to the spectral-vanishing property of the proposed residual-based artificial viscosity model.

With such dissipation term, the present stabilized RAV-HOS algorithm has been built with an operator-splitting strategy to keep its explicit property. For a certain sub-stage in Eq.(15), it follows

$$\begin{aligned} \Psi^* &= \Psi^{(i)} + \frac{\partial \Psi^{(i)}}{\partial t}\delta t, \\ \Psi^{**} &= \Psi^* + D(\Psi^{**})\delta t, \\ \Psi^{(i+1)} &= \gamma\Psi^{(0)} + (1-\gamma)\Psi^{**}, \end{aligned} \tag{24}$$

where implicit Euler scheme has been adopted for the stabilization-step, which can be easily resolved in the wave-number space because of its linear property about Ψ^{**}, and γ depends on the corresponding sub-stage within Runge-Kutta scheme.

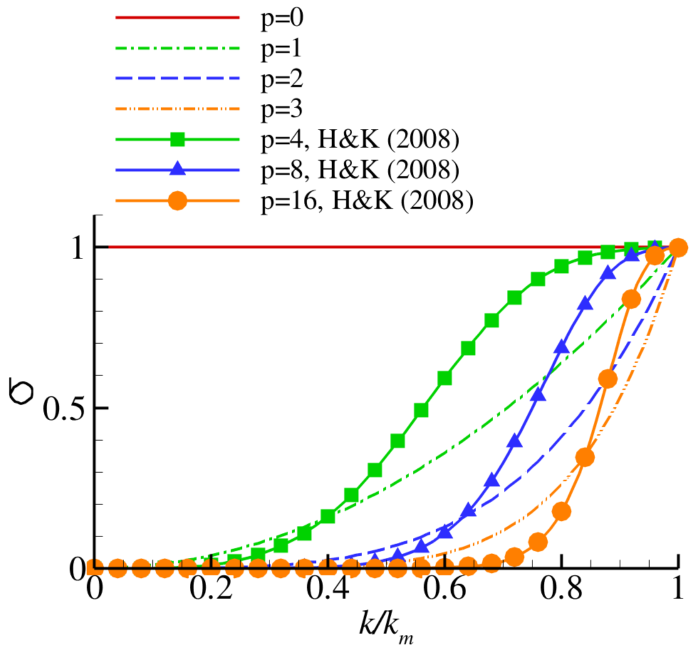

Fig. 2. Strength of the present spectral-filter with $p = 0 - 3$ ($2p = 0 - 6$) and the enhanced exponential filter with $p = 4 - 16$ from Hesthaven and Kirby (2008) (H&K).

Furthermore, for $\Psi^{(1)}$-predictor, $\Psi^{(n)}$, $\Psi^{(n-1)}$, ... have been adopted for temporal polynomial fitting with constant δt. While, for $\Psi^{(2)}$- and $\Psi^{(3)}$-predictors, $\Psi^{(1)}(\Psi^{(2)}),\Psi^{(n)}$,... have been used with the first temporal increment δt and $0.5\delta t$ respectively. Except the solitary wave simulation with larger amplitudes in Sec. 4.2.1 ($\frac{A_0}{d} \geq 0.9$), the dissipation parametre β has been set as $\beta = (2\pi)^2$.

4 Numerical Results

In the previous sections, the overall numerical algorithms for the proposed RAV-HOS model have been presented. In this section, numerical simulations with the present potential-based stabilized free-surface model will be carried out to check the relating efficiency and accuracy.

4.1 Wave Sloshing in a Rectangular Tank

4.1.1 Two Dimensional Free Sloshing with Single-Mode Initial Profile

Firstly, to confirm the accuracy of the present RAV-HOS model, two dimensional sloshing in a rectangular tank has been simulated. To launch the gravity-driven free sloshing without external excitation, the initial profile of the free-surface has been set as its 2_{nd} natural mode, i.e., $\eta(x, 0) = acos(2\pi(x - x_0)/l)$, with l the width of the tank. To check both linear and nonlinear performance of the model, three sets of $a/d = 0.001 - 0.100$ have been adopted and the mid-tank wave elevation has been shown in Fig. 3(b), where t has been normalized with $\sqrt{g/d}^{-1}$.

As it can be observed in Fig. 3(b), the present RAV-HOS model has shown satisfactory performance for such single-mode free sloshing problem. As it has been expected, when the initial wave amplitude a/d is small, linear behaviour has been obtained. In this case, the natural frequency of free-surface motion can be well-approximated by $\omega_2^2 = gk_2tanh(k_2d)$, with $k_2 = \frac{2\pi}{l}$. As shown in Fig. 3(b), for such linear case, obvious agreement has been reached for both wave amplitude and oscillation frequency. With the increase of a/d, the nonlinearity of the fluid sloshing becomes dominant. In this case, the temporal symmetry of wave elevation has been broken, because of the mode-coupling between different eigen-modes.

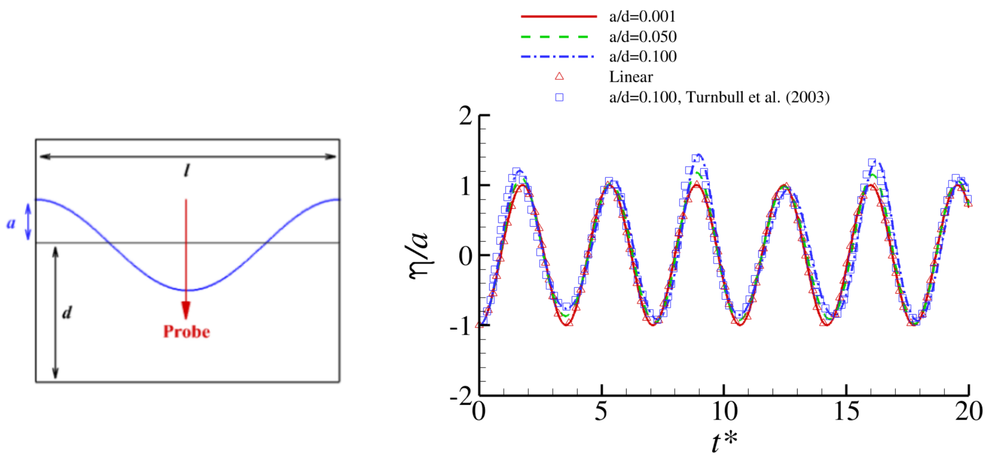

(a) (b)

Fig. 3. Sketch of the 2D free sloshing in a rectangular container with 2_{nd} natural mode as the initial condition ((a)), and the prediction about normalized mid-tank free-surface elevation ((b)).

With such wave-wave interaction, which can be omitted for the linear case, non-periodical behaviour can be observed. In Turnbull et al. (2003), to capture such nonlinear behaviour of fluid motion, σ-coordinate-transformation-based Finite Element model has been developed. It can be observed that the present results match well with their nonlinear FEM ones.

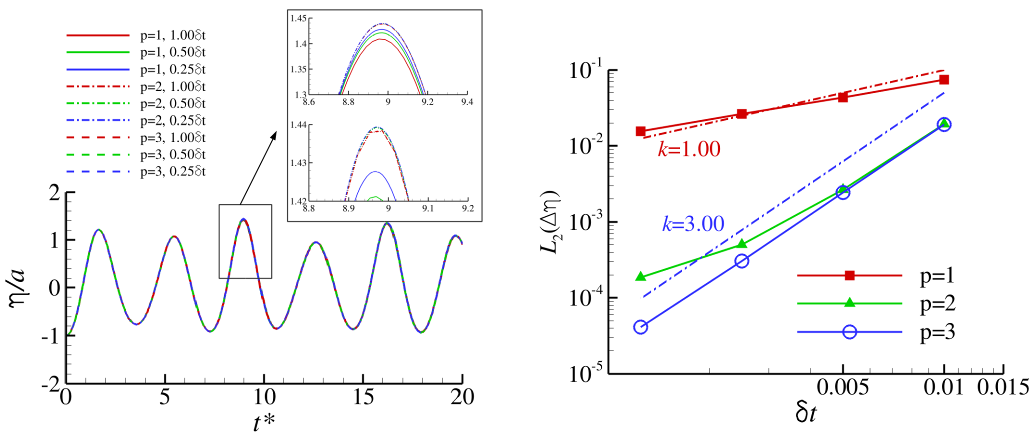

(a) (b)

Fig. 4. Free-surface predictions with the present RAV-HOS model for 2_{nd} mode free sloshing ($a/d = 0.100$, $p = 1-3$) ((a)) and the convergence performance based on Richardson estimation ((b)).

In the present research, details about the selection for BDF-order has been omitted and has been left as our future research topic. Presently, backward Euler scheme has been adopted and the local error is $O(\delta t^2)$, which is inconsistent with the $O(\delta t^4)$ one for TVD-RK3 integrator. To check how such lower-order residual estimation affects the numerical accuracy of the free-surface prediction, Fig. 4(a) shows the convergence performance of the present RAV-HOS model for mode-2 sloshing with $a/d = 0.100$ and it can be observed that the overall performance of the model is satisfactory with consistent prediction about the wave elevation without noticeable difference. As it has been mentioned in Sec. 3.2, free parametre $p = 1, 2, ...$ exists to enhance the performance of artificial dissipation. In compressible flow simulation, such parametre has been set as $p = 1$ to match the physical viscous effect. Following Eq. (23), in the wave-number space, with the well-evaluated numerical residual $\tilde{Res}$, the normalized wave-numbers $(\frac{k_x}{k_{x,max}})^{2p}$ and $(\frac{k_y}{k_{y,max}})^{2p}$ act as the spectral-filters ranging from 0 to 1, as shown in Fig. 2. With the increase of p, such filter in lower-wave-number region tends to 0 rapidly. As shown in Fig. 4(a), for the traditional selection of $p = 1$, the appearance of the additional dissipation has broke the $O(\delta t^4)$ local convergence, i.e., the $O(\delta t^3)$ global convergence, of the TVD-RK3 scheme. For TVD-RK3 integrator, although only $O(\delta t^2)$ local accuracy can be obtained for the auxiliary Euler-predictors, the weight factors in Eq. (15) have been designed with care to cancel-out such residuals to reach the overall $O(\delta t^4)$ local accuracy, considering the coupling between Euler-predictors in detail. Within the present RAV-HOS model, such coupling has been disregarded during the estimation about the artificial dissipation. Therefore, additional errors have been introduced to break the $O(\delta t^4)$ local accuracy of the TVD-RK3 predictor. To confirm such hypothesis, convergence histories have been obtained as shown in Fig. 4(b). Because of the unavailability for the 'exact' free-surface motion, Richardson-algorithm has been adopted to estimate the convergence rate, as it has been recommended by Celik et al. (2008). As it has been expected, only $O(\delta t)$ global accuracy ($O(\delta t^2)$ local accuracy) can be reached for $p = 1$ cases. With the increase of $p = 2$, the convergence performance of such explicit 3_{rd}-order integrator has been reproduced , as the result of vanishing dissipation for lower-wave-number wave components. For such mode-2 sloshing, dominant contribution from lower-wave-number components ($\frac{k_x}{k_{x,max}} \ll 1$) can be expected. Therefore, a further increase of $p = 3$ makes no obvious improvement about the results. Generally speaking, for the consideration about temporal convergence, $p = 2$ is preferred and such configuration, together with the residual estimation with 1_{st} order backward Euler formula, have been adopted in the remaining parts of the present work, unless otherwise stated.

4.1.2 Three Dimensional Free Sloshing with Gauss-Shaped Initial Profile

As it has been simulated in Sec. 4.1.1, during the initial stage, the lower-order single-mode profile has been selected. Because of the nonlinear property of wave sloshing and the corresponding nonlinear mode-coupling, higher-order-modes have been activated, despite of their weaker strength to the main mode. With the present artificial dissipation strategy, lower dissipation occurs within the well-resolved lower-wave-number region, while such artificial energy-suppression becomes dominant with the increase of wave-number. To confirm how the artificial viscous term affects the wave behaviour within the higher-wave-number region, 3D wave sloshing free from excitation has also been simulated in this section.

In this part, general Gauss-shaped wave profile $\eta(x, y, 0) = H_0 e^{-\kappa r^2}$, where $r = \sqrt{(x - x_c)^2 + (y - y_c)^2}$ with (x_c, y_c) the free-surface centre, has been adopted as the initial condition (Wei and Kirby, 1995; Kang and Sotiropoulos, 2012). To confirm both the accuracy and dissipation performance of the present RAV algorithm, linear results have also been shown. For the present nonlinear HOS model, linear behaviour can be reached with an initial wave amplitude small enough, i.e., $H_0/L = 0.005$ with the width of the square-shaped container $L = 20m$. Consistent with Kang and Sotiropoulos (2012), the water depth in this section has been set as $D = 1.0m$, and the remaining parametres are $\kappa = 0.25/m^2$ and $g = 9.8m/s^2$. As shown in Figs. 5 and 6, with both the spectral-filtering and the present residual-based artificial viscosity models, reasonable numerical results have been obtained, but with different accuracy. For the spectral-filtering strategy and its extension, the sensitivity about the filtering parametres to the numerical results has been observed, as shown in Fig. 5. As it has been discussed in Sec. 3.2, the lack of coupling between dissipation rate and the temporal increment leads to the over-dissipation of the model, especially with small δt (Fig. 5(a)). With the decrease of δt, during the numerical simulation within a fixed temporal duration, the increase of filtering iterations, which can be approximated as $\frac{\Delta T}{\delta t}$, is believed to be the main source of the observed over-dissipation, as it has been mentioned in Sec. 3.2. To confirm such hypothesis, as shown in Fig. 5(c), with certain δt ($0.50\delta t$ case in Fig. 5(a)), the filtering interval has been increased to $\Delta n = 5$ and $\Delta n = 10$. As it can be observed, obvious improvement has been reached with such parametre optimization. Furthermore, as shown in Fig. 5(b), the numerical results also show sensitivity to the filtering strength

α_s. As it can be observed from Eqs. (16) and (17), the numerical dissipation is defined by the normalized wave-number. With the decrease of such normalized wave-number, vanishing artificial dissipation can be obtained. With the increase of grid resolution, as shown in Fig. 5(d), obvious improvement has been reached about the free-surface prediction, because of the larger normalization wave-number, which demonstrates the necessity of enough wave components for an acceptable numerical dissipation with the spectral-filtering based free-surface stabilization. Generally speaking, for the commonly-used spectral-filtering strategy for stability enhancement about the free-surface flow simulation, model parametres should be designed carefully to avoid the over-dissipation. Compared with the spectral-filtering model, the present residual-based artificial viscosity model shows attractive convergence performance. As shown in Fig. 6, the temporal increment shows no obvious effect on the numerical prediction about the free-surface elevation, because of its adaptive coupling to the artificial dissipation as it has been mentioned in Sec. 3.2. As another free parametre, consistent with Sec. 4.1.1, the numerical results are also not sensitive to the dissipation order, because of its spectral-vanishing property. As shown in Fig. 6(d), compared with the spectral-filtering approach, even with the coarse free-surface discretization, satisfactory free-surface prediction can be also obtained with the proposed residual-based stabilization strategy, and such property is attractive for potential efficiency improvement without the introduction of redundant wave components to achieve dissipation optimization within the spectral-filtering algorithm. Although the present case is quite a special one, it still shows the performance enhancement of the present adaptive artificial dissipation model to the traditional one with spectral-filtering.

4.1.3 Two Dimensional Forced Sloshing in a Rectangular Tank

Within the previous sections, free sloshing has been simulated to confirm the performance enhancement of the present RAV-HOS model to the traditional spectral-filtering one. In the fields of both academic research and realistic industrial application, compared with the free sloshing, the forced sloshing caused by either container oscillation or even earthquake is always an attractive topic. In this section, 2D forced sloshing within a rectangular container has been simulated to further confirm the performance of the present stabilized free-surface model. To model the wave sloshing within a container with forced oscillation, the boundary condition on the container surface becomes non-homogeneous. Within the present RAV-HOS model, such non-homogeneous BCs lead to the failure of eigen-expansion with double Fourier-modes. To remedy such inconsistency, the wave sloshing has been modelled with the container-fixed coordinate system. With such coordinate transformation, the local flow-potential also satisfies Eq. (5) and the local wave elevation follows Eq. (1), while Eq. (2) should be modified to consider the effect of container motion

$$\frac{\partial \eta_l}{\partial t} + \nabla_h \eta_l \cdot \nabla_h \phi_l = \phi_{l,z}, \tag{25}$$

$$\frac{\partial \phi_l}{\partial t} + \frac{\nabla \phi_l \cdot \nabla \phi_l}{2} + a_x x_l + a_y y_l + (g + a_z)\eta_l = 0, \tag{26}$$

where $a_{x,y,z}$ denote the container accelerations. Similar with the previous discussion, such formulas can be further transformed to their Zakharov's forms without difficulties.

Firstly, wave sloshing within a container oscillating horizontally with $0.0186sin(0.999\omega_1 t)$ has been simulated, where ω_1 denotes the 1_{st} order eigen-frequency $\omega_1^2 = gk_1 tanh(k_1 d)$ with $k_1 = \frac{\pi}{l}$ and $l/h = 2$. For accuracy confirmation, wave profiles at $t^* = 13.0667$ and $t^* = 15.725$ have been shown in Fig. 7. According to the linear theory, with the excitation frequency matching that of the eigen-mode, the single-mode resonance can be obtained. As shown in Figs. 7(a) and 7(b), because of such resonance, the increase of wave elevation leads to the nonlinear behaviour of the free-surface. Even with such small amplitude oscillation, the symmetry-breaking of the large amplitude response still occurs. It can be observed that the present results match well with both the experimental and numerical results from Okamoto and Kawahara (1990) and Shao and Faltinsen (2014).

Other than the horizontal excitation, vertical component of the container motion has also been considered in this

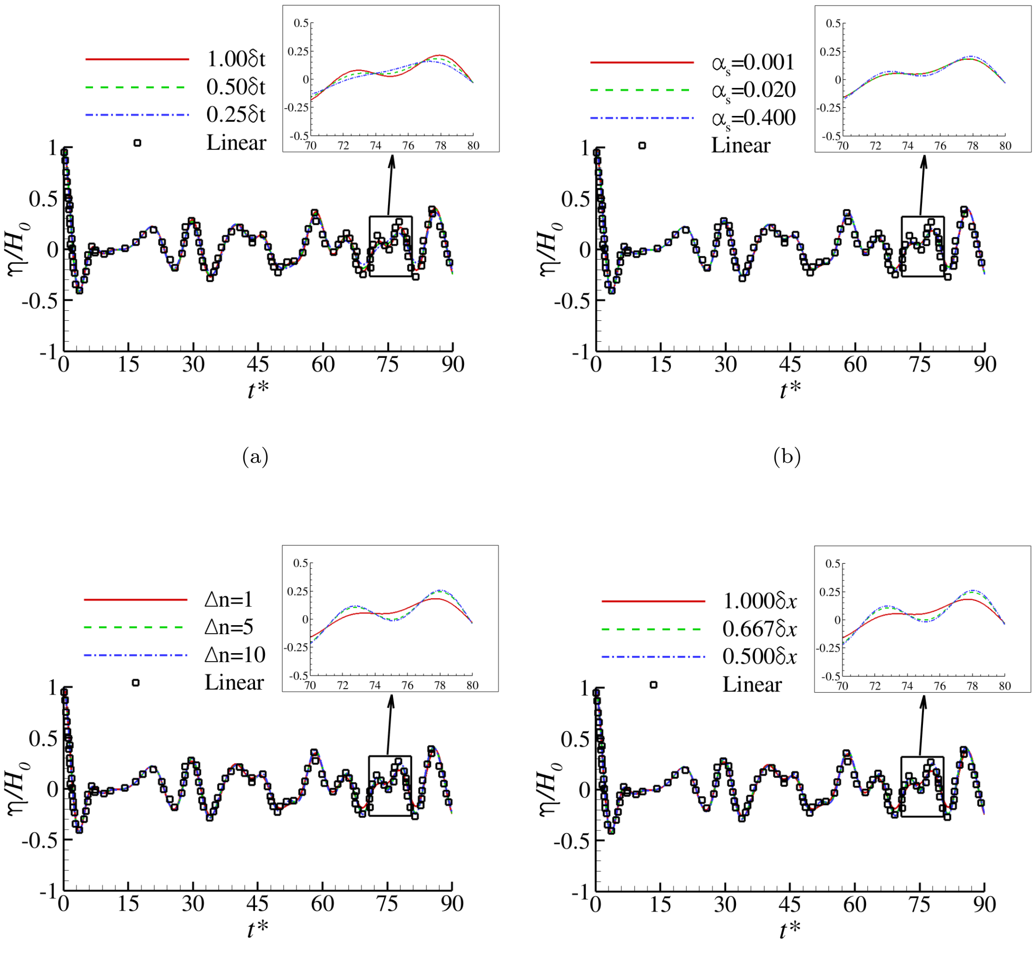

Fig. 5. Free-surface elevation for Gauss-shaped free sloshing about the container centre with different filtering strategies: (a) $\Delta n = 1$ with filter Eq. (16); (b) $\Delta n = 1$ with filter Eq. (17); (c) multi-step filtering with filter Eq. (16); (d) identical to (a) with various spacial configurations.

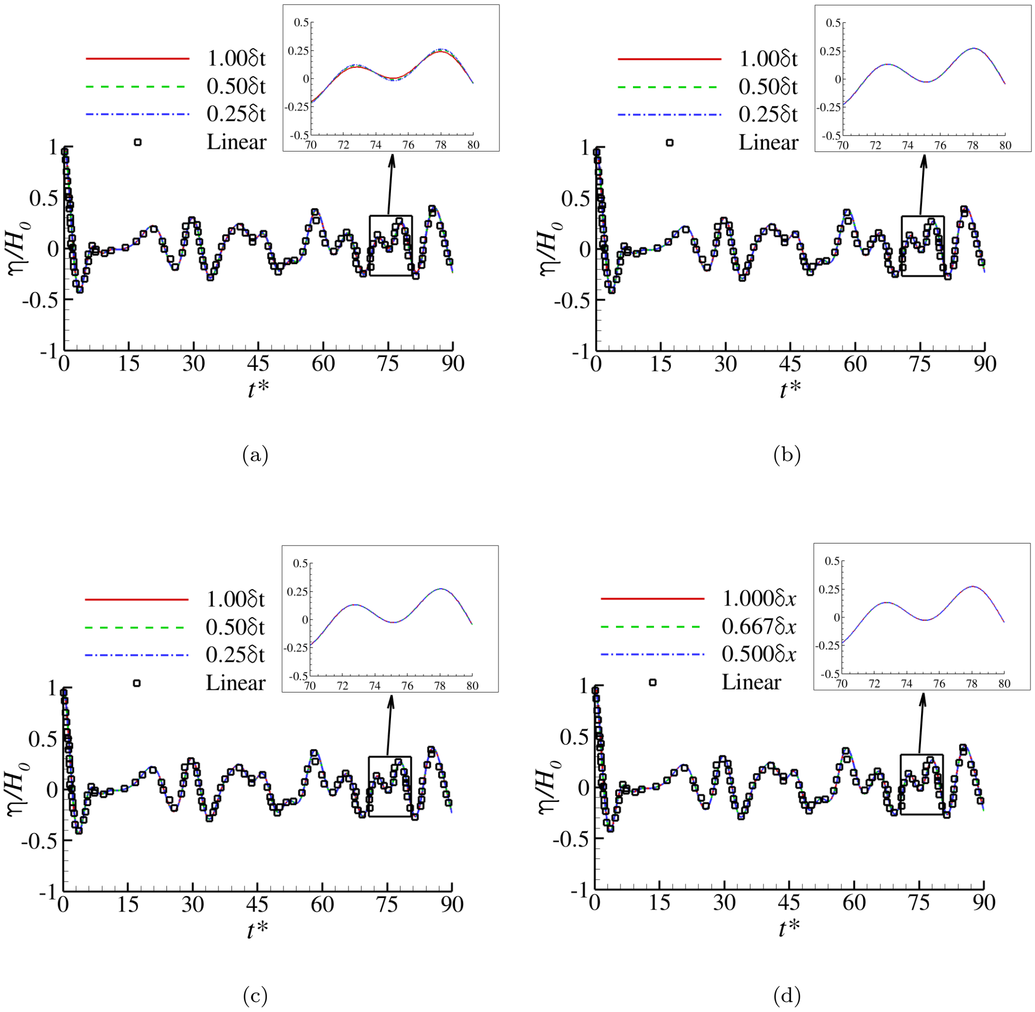

Fig. 6. Free-surface elevation for Gauss-shaped free sloshing about the container centre with different residual-based artificial viscosity orders: (a) $p = 1$; (b) $p = 2$; (c) $p = 3$; (d) identical to (b) with various spacial configurations.

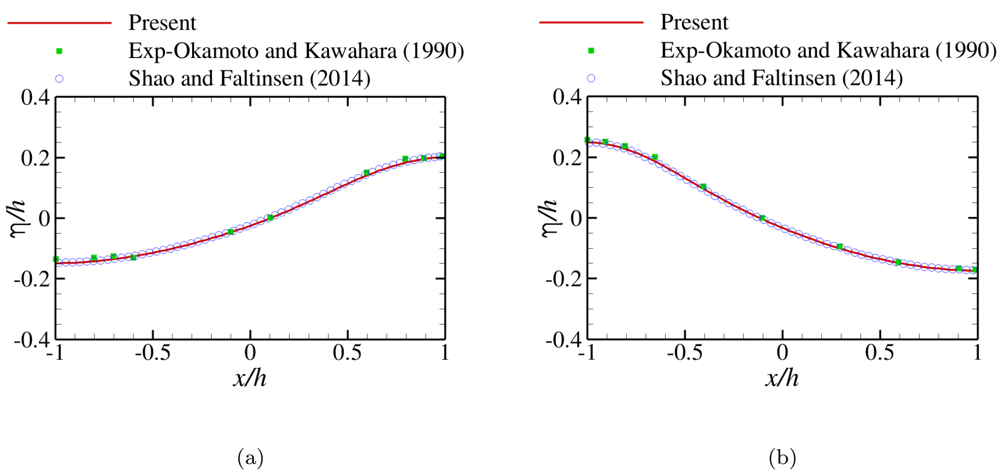

Fig. 7. Free-surface profiles for 2D forced sloshing within a rectangular container at (a) $t^* = 13.0667$ and (b) $t^* = 15.725$.

section. Consistent with Frandsen (2004), purely vertical excited sloshing (case I) with $k_v = 0.5$, $\frac{\omega_v}{\omega_1} = 0.798$, $\epsilon = 0.0014$ and $k_v = 0.5$, $\frac{\omega_v}{\omega_1} = 0.798$ coupled with $k_h = 0.0014$, $\frac{\omega_h}{\omega_1} = 0.98$ and $\epsilon = 0.0$ (case II) have been simulated, where the details about parametre definition can be found in Frandsen (2004). It can be observed from Fig. 8 that for both cases, the present prediction about the free-surface elevation matches well with that obtained by the FDM model from Frandsen (2004), and for case II, the resonance property of the horizontal mode leads to the large amplitude wave motion.

According to the above results for liquid sloshing, the accuracy and performance enhancement of the present RAV-HOS model has been confirmed. In the next section, the present stabilized free-surface model will be adopted as the flow-resolving component of the Numerical-Wave-Tank for wave simulation.

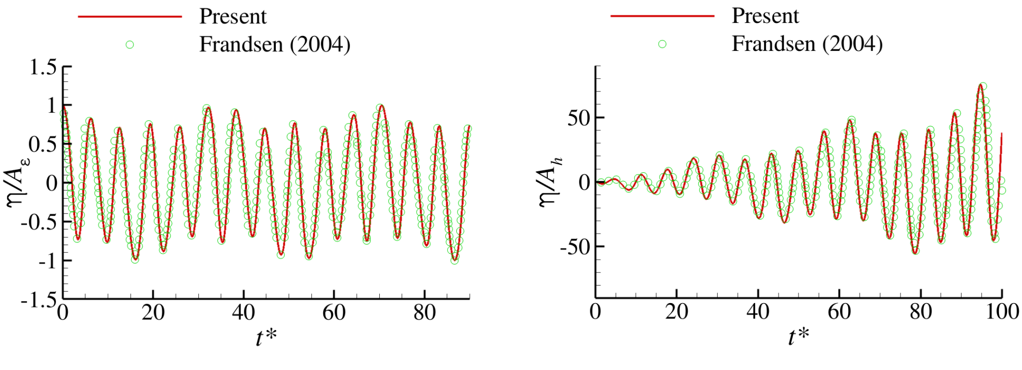

(a) (b)

Fig. 8. Free-surface elevation for 2D forced sloshing within a rectangular container with (a) horizontal excitation (case I) and (b) coupled vertical-horizontal excitation (case II).

4.2 RAV-HOS based Numerical-Wave-Tank (RAV-HOS-NWT)

As it has been discussed in Sec. 4.1, the present residual-based artificial dissipation acts as an adaptive spectral-filter to enhance the numerical performance of the HOS-based free-surface model, while remaining its accuracy. In this section, the developed RAV-HOS model will be adopted for the development of the Numerical-Wave-Tank (NWT), which has been commonly-used in the field of offshore and oceanic hydrodynamic research.

4.2.1 Solitary Wave Generation

As the first step for the NWT development, wave run-up of solitary wave has been simulated to check the performance of the present RAV-HOS model for long-range wave propagation. To launch the solitary wave evolution, initial free-surface profile has been set as $\eta(x,0) = \frac{A_w}{cosh^2(\sqrt{\frac{3}{4}\frac{A_w}{d}}\frac{x}{d})}$ (Lin et al., 2005). To evaluate the amplitude of the solitary wave within a NWT with $L/d = 20.0$, the wave-peak at $x/d = 10.0$ has been extracted as A_0. As shown in Fig. 9(a), for such shallow-water case, the wave velocity can be approximated well with $c = \sqrt{gd}$. For $t^* > 6.0$, solitary wave can be obtained, which confirms the reliability for the selection of mid-tank wave-peak as the solitary wave scale. With the increase of A_w, wave tail becomes obvious (Figs. 9(b) and 9(c)). As it will be discussed later, the increase of wave velocity leads to earlier wave reflection compared with the smaller amplitude case (Fig. 9(a)). As it can be observed, the complex behaviour of solitary wave has been enhanced with the increase of wave amplitude. Actually, during the solitary-wave-generation with piston-type wave-makers, similar wave tails have also been observed, as it has been mentioned in Tong et al. (2019). During their wave-making processes, such flow behaviour can be traced back to the inconsistent definition about the inlet boundary-condition and the unwanted wave components can be removed with the piston-type inlet-boundary replaced by a stationary one with fully-nonlinear solitary wave elevation and horizontal velocity profile (Clamond and Dutykh, 2013) as the boundary conditions. During the present solitary-wave-generation, the source of the wave tail is different. In the present simulation, the initial wave profile has been set as the analytical solution from Laitone (1960) with vanishing flow velocity in the fluid domain. For the shallow water cases, the wave evolution can be obtained by $\eta(x,t) = \frac{\hat{\eta}(x-ct)+\hat{\eta}(x+ct)}{2}$ with $\hat{\eta}(x)$ the reflection of initial wave profile about $x/d = 20.0$ followed by its periodical extension. As it can be observed in Fig. 9(a), when the initial wave amplitude is small, the wave profiles match the shallow water ones well. With the increase of A_w, both the nonlinearity ($\frac{A_w}{d}$) and dispersibility ($\frac{d}{L_w}$) increase. The nonlinearity leads to the increase of wave velocity, while the dispersibility leads to the separation of long- and short-Fourier-wave-components. With a larger A_w, the initial wave profile becomes narrower, leading to more Fourier-wave-components within the initial wave elevation. It is believed that the dispersibility leads to the separation of Fourier-wave-components and the formation of complex wave tail, while the nonlinearity leads to a faster wave-travelling (Figs. 9(a) - 9(c)). Furthermore, with the Fourier-wave-separation, the Linear-Shallow-Water-Equation (LSWE) over-estimates the solitary-wave-amplitude, as shown in Figs. 9(b) and 9(c), because of the energy transfer. Although such topic is attractive, it is obvious beyond the goal of present research and will not be discussed further. As shown in Fig. 9(d), the present results about solitary wave run-up match well with the previous ones (Chan and Street, 1970; Yue et al., 2003; Lin et al., 2005). With the adopted wave amplitudes, linear behaviour about the wave run-up has been observed, which can be traced back to the long-wave property of the wave motion. With such validation, preliminary confirmation about the feasibility of the present RAV-HOS model as the flow solver for NWT has been reached.

4.2.2 Regular and Irregular Focus Wave Generation

Uppon the solitary wave, in this section, wave-maker has been equipped to the RAV-HOS-NWT for both regular and irregular wave simulation. As it has been discussed in Clamond et al. (2005), compared with the relaxation-zone approach, pneumatic wave-maker shows much better performance. In the present research, linear wave-making theory has been adopted to match such pressure distribution to the far-field wave generation (Clamond et al., 2005). For multichromatic wave with N components, superposition of wave-making pressure sources has been carried out following

$$\frac{P_G}{\rho} = \Sigma_{i=1}^{N} sin(\omega_i t + \theta_i) P_i(x), \tag{27}$$

$$P_i(x) = gA_i\sqrt{\frac{e}{2\pi}}(1 + \frac{2k_i d}{sinh(2k_i d)})e^{-x^2/2\lambda_i^2}, \tag{28}$$

where the wave number k_i follows the dispersion relationship with ω_i by $\omega_i^2 = gk_i tanh(k_i d)$, θ_i denotes the wave phase and $\lambda_i = k_i^{-1}$. During the present numerical simulations, it has been observed that the mentioned linear wave-making theory works well for small wave amplitude cases. With the increase of wave amplitude, undesirable higher-order wave deformation has been encountered, leading to the failure of large amplitude wave-making and such an issue has been left as one of our future research directions. Although such issue exists, for the focus wave, because of the wave focusing at the focal point far away from the wave-making zone, linear behaviour around the wave-maker has been observed, leading to the feasibility of focus wave generation with the present linear wave-making model.

Firstly, two sets of regular waves have been simulated as the preparation for the irregular focus ones. In this part, constant water depth of $d = 0.7m$ has been adopted to reproduce the experimental work about wave-focusing by Baldock et al. (1996) and the corresponding numerical simulation from Johannessen and Swan (1997). For the regular waves, $T = 1.4s$ and $T = 0.6s$ cases with $A = 0.005m$ are selected to check the performance of the present RAV-HOS-NWT. Furthermore, with these two simulations, focal point and focal time are determined to guaranteen that all the wave components for the following irregular focus wave simulation have been well developed. As shown in Fig. 10, both the wave histories at $x = 5.0m$ and $x = 10.0m$ for $T = 1.4s$ case match well with the nonlinear 5_{th} order Stokes' solution.

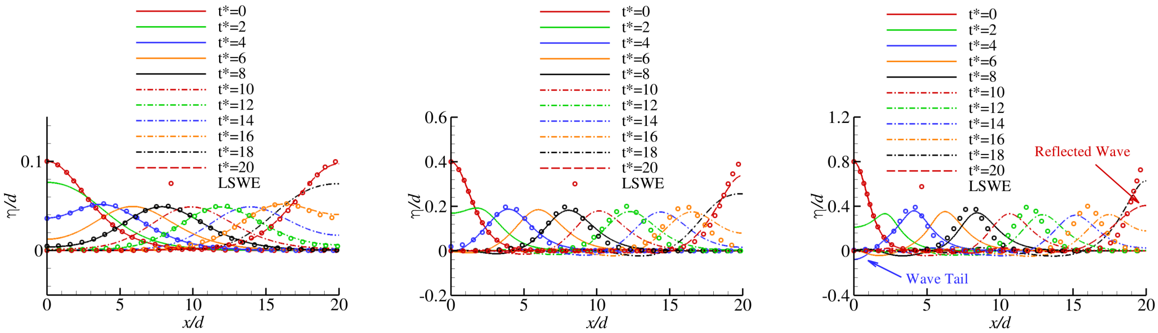

(a) (b) (c)

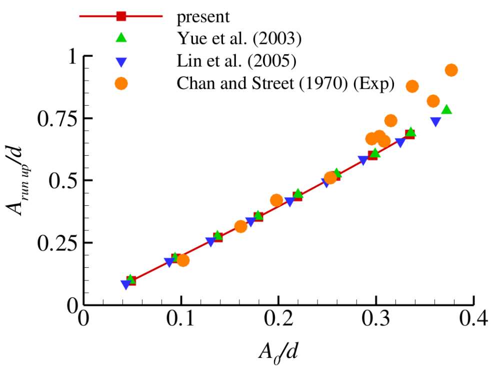

(d)

Fig. 9. Wave profiles and wave run-up for 2D solitary wave caused by initial wave elevation: (a) $A_w/d = 0.10$; (b) $A_w/d = 0.40$; (c) $A_w/d = 0.80$; (d) wave run-up on the right side-wall $x/d = 20.0$ and its comparison with previous experimental and numerical results.

For such wave configuration, the wave steepness is small compared with that of $T = 0.6s$ case. As it can be observed from Fig. 10(b), the wave length and wave phase also match the theoretical ones well. Furthermore, as shown in Fig. 11, the wave histories (Fig. 11(a)) and wave profile (Fig. 11(b)) for a shorter wave with $T = 0.6s$ have also been simulated with the present RAV-HOS-NWT model. With the increase of wave steepness, the performance of the present model is also satisfactory.

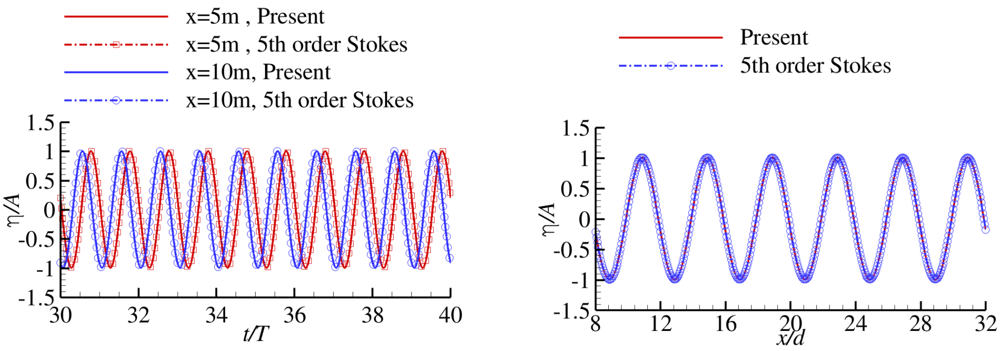

(a) (b)

Fig. 10. Time history of wave elevation and the free-surface profile for 2D regular wave with $T = 1.4s$.

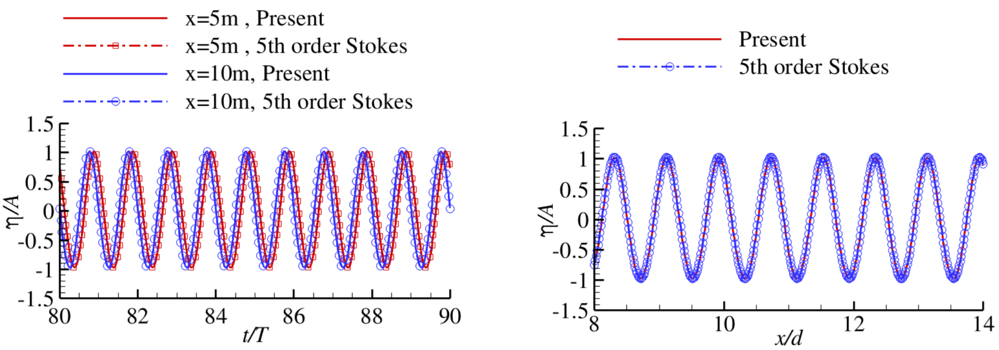

(a) (b)

Fig. 11. Time history of wave elevation and the free-surface profile for 2D regular wave with $T = 0.6s$.

In recent years, focus waves have become one of the popular topics for oceanic and offshore engineering, due to the rich flow physics it contains and the potential damages to the marine structures. Adopting the phase superposition algorithm, in this section, two sets of focus waves (case B and case D), which have also been reported in Baldock et al. (1996) and Johannessen and Swan (1997), have been reproduced for performance confirmation about the RAV-HOS-NWT model. To launch such irregular focus wave simulation, total wave amplitude $A = 0.055m$ has been divided into 29 wave components with case B: $0.6s \leq T \leq 1.4s$ and case D: $0.8s \leq T \leq 1.2s$. As it has been shown for regular waves, focal time $t_f = 50.0s$ and focal location $x_f = 10.0m$ have been selected for the adequate growth of all the wave components.

It should be mentioned that, with the nonlinear wave-wave interactions during propagation, the focal time and

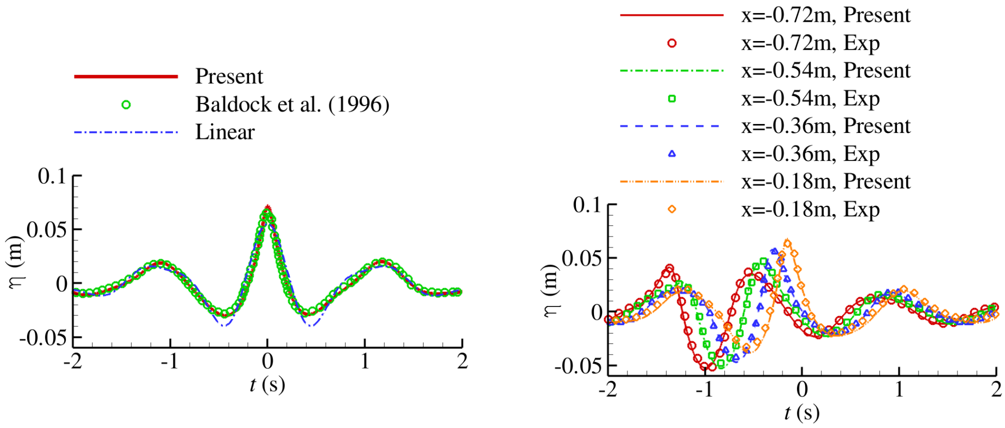

(a) focal point

(b) upstream side

Fig. 12. Time history of 2D focus wave elevation for case B with $0.6s \leq T \leq 1.4s$.

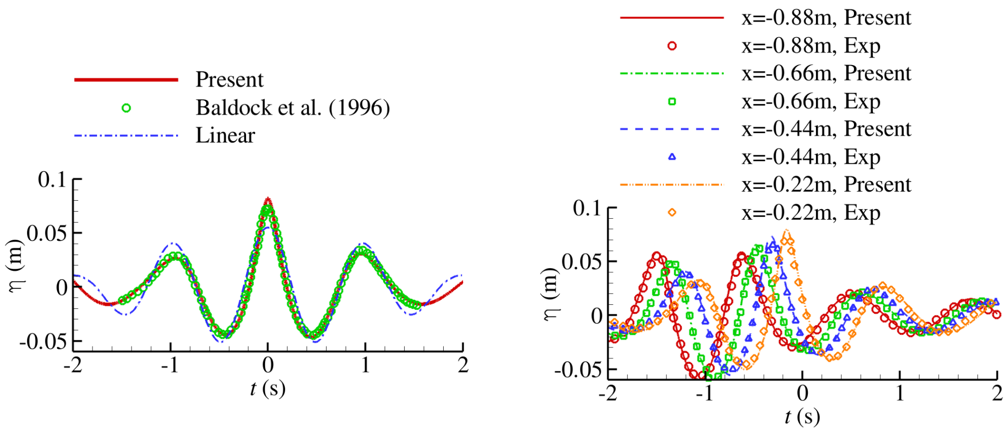

(a) focal point

(b) upstream side

Fig. 13. Time history of 2D focus wave elevation for case D with $0.8s \leq T \leq 1.2s$.

focal location of the focus wave will be different from the linear ones. In this section, the numerical results at the real focal point have been shifted to make the focal time $t_f = 0$. As it can be observed from Figs. 12 and 13, the present predictions about the wave elevation match well with the experimental ones from Baldock et al. (1996). Because of the nonlinearity, the wave elevation shows difference from the linear one. For the peak, the linear model under-estimates the wave amplitude and for the trough, such wave elevation has been over-estimated. Generally speaking, the present RAV-HOS-NWT model has produced accurate predictions about the nonlinear focus wave elevation with over-estimation about the focus-wave-peak compared with the experimental results, and such difference can be probably traced back to the rough selection about the focal location and the focal time within the present numerical configuration.

4.2.3 Ship-Wave Generation

Lastly, other than the 2D wave-simulations with the present RAV-HOS-NWT model, 3D simulations about the ship-wave with moving pressure source have also been carried out. Consistent with Clamond et al. (2005), a local pressure source in the form $\frac{P_G}{\rho} = p_0 - \bar{p}_0$ with $p_0 = Ae^{-(\frac{x^2}{\lambda_x^2}+\frac{y^2}{\lambda_y^2})}$ has been added to Eq. (4). On the other hand, other than the moving pressure on the fixed free-surface, coordinate transformation has been carried out in this section to make the moving pressure source a fixed one. To remedy the relating inconsistency in the definition about the $\frac{D(\cdot)}{Dt}$ term, both Eqs. (3) and (4) are modified to their ALE forms with $\frac{D(\cdot)}{Dt} = \frac{\partial(\cdot)}{\partial t} + U_p \cdot \nabla_h(\cdot)$ with U_p the moving velocity of the free-surface pressure. Considering the spectral accuracy of the proposed double Fourier-expansions about both free-surface elevation and free-surface potential, unlike the commonly used upwind schemes to avoid negative dissipation, in the present work, the horizontal gradient operators within the mentioned ALE formulas have been achieved in a spectral way as it has been done in Sec. 3.1.

As shown in Fig. 14, the present RAV-HOS-NWT model has succeeded to reproduce the moving-pressure-caused ship-wave with $\lambda_x = \lambda_y = 1.0m$, $U_p = 1.0m/s$ and $A/g\lambda_x = 0.15$. As it has been discussed in Clamond et al. (2005), the initial wave profile is a local trough because of its initial hydro-static balancing with the pressure distribution. Therefore, with the moving of such pressure source, a ring-like profile has been obtained. As shown in Figs. 14(b)-14(e), the wave length of such ring-like wave is smaller compared with the main ship-wave profile. With the moving of free-surface pressure, both long- and short-waves have been captured well with the present RAV-HOS model, due to its spectral accuracy and the relating high resolution. Furthermore, at the end of the simulation with $t^* = 100$, the sliced wave elevation has been compared with that from Clamond et al. (2005) by the spectral BEM model (Fig. 15). With the re-definition about x-coordinate, all the sliced wave profiles match well with the previous ones, even for the steep-wave right behind the pressure source, which further confirms the capacity of the present stabilized free-surface model for large-scale wave simulation.

5 Conclusions

In the present research, a stabilized High-Order Spectral (HOS) model has been developed for an efficient prediction about fully-nonlinear free-surface flow. To enhance the numerical performance of the model, a residual-based artificial viscosity has been adopted to achieve artificial dissipation for under-resolved wave components adaptively. Within the proposed stabilization algorithm, spectral-vanishing property has been produced, with the additional dissipation scaled with wave-numeber bound and the normalized numerical residual, which has been estimated with a Backward Differentiation Formula (BDF) in the time-domain. With the coupling of such dissipation to the temporal increment δt with certain dissipation order p, the proposed energy-suppression strategy acts as an adaptive spectral filter. With such δt-related filtering, convergence enhancement has been reached, compared with the commonly-used spectral-filtering approach. Furthermore, it has been shown that the dissipation order p plays an important role to suppress the undesirable energy-decaying for well-resolved wave components with lower wave-numbers. To check the performance of the proposed

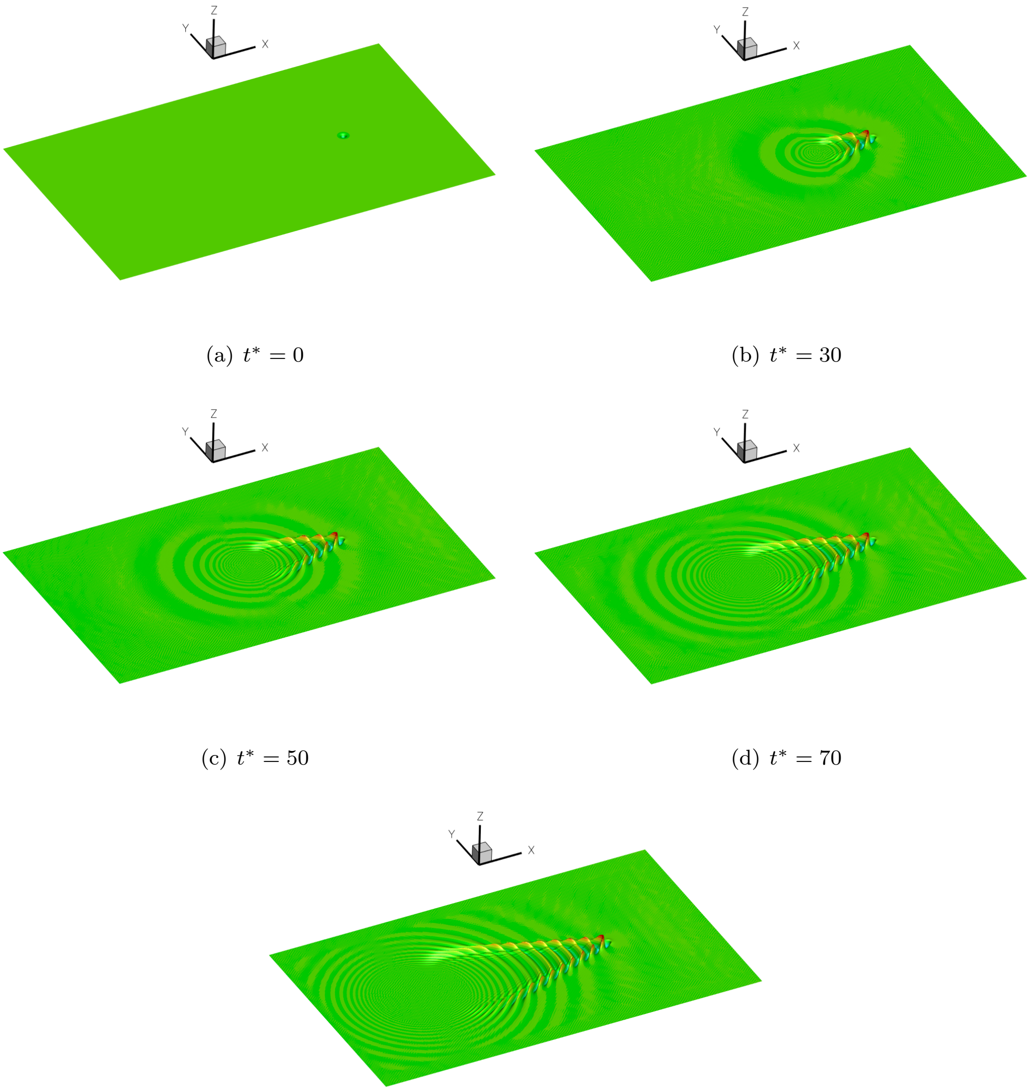

(a) $t^* = 0$

(b) $t^* = 30$

(c) $t^* = 50$

(d) $t^* = 70$

(e) $t^* = 100$

Fig. 14. Wave profiles for the ship-wave modelled with the moving pressure source at $t^* = 0 - 100$.

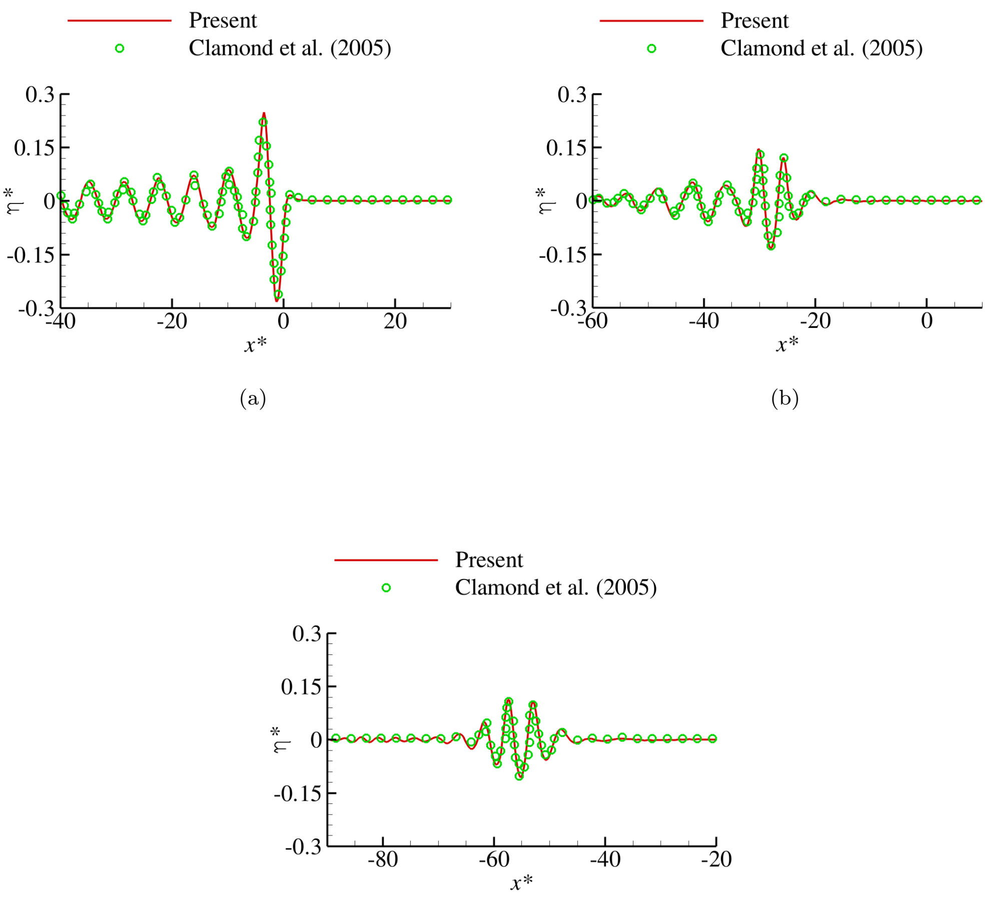

(c)

Fig. 15. Wave elevation for the ship-wave modelled with the moving pressure source at $t^* = 100$ and (a) $y^* = 0$, (b) $y^* = 10$, (c) $y^* = 20$.

RAV-HOS model, liquid sloshing has been simulated, which confirms both accuracy and robustness of the present artificial dissipation algorithm. For its extension to wave-wave and further wave-structure interactions, a Numerical-Wave-Tank (NWT) has been built with the pneumatic wave-making theory. With the reproduction about the evolution of solitary waves, regular waves, irregular focus waves and further ship-waves, it demonstrates the feasibility for the application of our RAV-HOS-NWT model to oceanic, offshore and marine engineering researches. Even the present model is still in its series version, the overall algorithm can be extended to its parallel one without technical difficulties.

Acknowledgements

The present research has been financially supported by the Fundamental Research Funds for the Central Universities (Grant No.3132024220), the National Natural Science Foundation of China (Grant No.52271261) and the National Key Research and Development Program of China (Grant No.2021YFB2601102). These supports are gratefully acknowledged.

Data Availability Statement

Data sets generated during the current study are available from the corresponding author on request.

Appendix

As it has been discussed in Sec. 3.2, $\left|\tilde{\psi}\right|$ has been adopted as the normalization factor to achieve dimension-balancing for the artificial viscosity. In this section, the rationality about such choice will be discussed preliminarily.

For a simple ODE with single DoF, e.g., $\dot{y} = R(y,t)$, its unconditional-stable implicit Euler predictor follows

$$\frac{y^{n+1} - y^n}{\delta t} = R(y^{n+1}, t^{n+1}). \tag{29}$$

While, for explicit Euler predictor, such explicit estimation about y^{n+1} (denoting as y^*) can be obtained as

$$\frac{y^* - y^n}{\delta t} = R(y^n, t^n), \tag{30}$$

which leads to a numerical residual of Eq. (29) as

$$\frac{y^* - y^n}{\delta t} = R(y^*, t^{n+1}) + Res. \tag{31}$$

With the assumption of $R_t \approx 0$, i.e., R varies slower than y itself with respect to t (available for higher-wave-number wave components in the present research, where t has been only explicitly-defined in external excitation), and the fact that $y^{n+1} - y^* = O(\delta t^2)$ (2_{nd} order temporal accuracy for both implicit and explicit Euler schemes), Eq. (29) can be reformulated as

$$\begin{aligned}\frac{y^{n+1} - y^n}{\delta t} &= R(y^n, t^{n+1}) + R(y^{n+1}, t^{n+1}) - R(y^n, t^{n+1}) \\ &= R(y^n, t^{n+1}) - Res + [R(y^{n+1}, t^{n+1}) - R(y^*, t^{n+1})] \\ &\approx R(y^n, t^{n+1}) - Res \\ &\approx R(y^n, t^n) - Res \\ &\approx R(y^n, t^n) - \frac{Res}{y^*} y^{n+1}.\end{aligned} \tag{32}$$

To make it always dissipative, the residual term should take its absolute value form $\frac{|Res|}{|y^*|}y^{n+1}$, leading to the rationality of the present residual normalization. Within the present RAV-HOS model for free-surface flow, in principle, such formula can be used in either physical space or wave-number space. Obviously, the mentioned numerical approximations in Eq. (32) have introduced considerable errors. Therefore, it should be used only for under-resolved wave components. Within the physical space, all the collocation grid points and the relating DoFs are equivalent and it is hard to determine which DoF has been well-resolved and which DoF has been under-resolved. In this way, such formula should be applied in the wave-number space, where the wave components with larger wave-number have been predicted with poor accuracy compared with smaller wave-number ones. Compared with Eq. (23), the normalized wave-number term acts as such spectral-vanishing filter to avoid the over-dissipation to the well-resolved wave components.

References

T. E. Baldock, C. Swan, P. H. Taylor, and F. T. Smith. A laboratory study of nonlinear surface waves on water. *Philosophical Transactions of the Royal Society of London. Series A: Mathematical, Physical and Engineering Sciences*, 354(1707):649–676, 1996.

H. B. Bingham and H. W. Zhang. On the accuracy of finite-difference solutions for nonlinear water waves. *Journal of Engineering Mathematics*, 58:211–228, 2007.

I. B. Celik, U. Ghia, P. J. Roache, C. J. Freitas, H. Coleman, and P. E. Raad. Procedure for estimation and reporting of uncertainty due to discretization in cfd applications. *Journal of Fluids Engineering*, 130(7):078001, 2008.

R. K. C. Chan and R. L. Street. A computer study of finite-amplitude water waves. *Journal of Computational Physics*, 6:68–94, 1970.

D. Clamond and D. Dutykh. Fast accurate computation of the fully nonlinear solitary surface gravity waves. *Computers and Fluids*, 84:35–38, 2013.

D. Clamond and J. Grue. A fast method for fully nonlinear water-wave computations. *Journal of Fluid Mechanics*, 447: 337–355, 2001.

D. Clamond, D. Fructus, J. Grue, and Ø Kristiansen. An efficient model for three-dimensional surface wave simulations. part ii: Generation and absorption. *Journal of Computational Physics*, 205:686–705, 05 2005.

E. J. R. Coutinho, M. Dall'Aqua, L. McClenny, M. Zhong, U. Braga-Neto, and E. Gildin. Physics-informed neural networks with adaptive localized artificial viscosity. *Journal of Computational Physics*, 489:112265, 2023.

W. Craig and C. Sulem. Numerical simulation of gravity waves. *Journal of Computational Physics*, 108(1):73–83, 1993.

T.A. Dao and M. Nazarov. A high-order residual-based viscosity finite element method for the ideal mhd equations. *Journal of Scientific Computing*, 92(3):77, 2022.

D. G. Dommermuth and D. K. P. Yue. A high-order spectral method for the study of nonlinear gravity waves. *Journal of Fluid Mechanics*, 184:267–288, 1987.

G. Ducrozet, F. Bonnefoy, D. Le Touzé, and P. Ferrant. A modified high-order spectral method for wavemaker modeling in a numerical wave tank. *European Journal of Mechanics - B/Fluids*, 34:19–34, 2012.

T. Dzanic and F. D. Witherden. Positivity-preserving entropy-based adaptive filtering for discontinuous spectral element methods. *Journal of Computational Physics*, 468:111501, 2022.

A. P. Engsig-Karup, H. B. Bingham, and O. Lindberg. An efficient flexible-order model for 3d nonlinear water waves. *Journal of Computational Physics*, 228(6):2100–2118, 2009.

A. P. Engsig-Karup, C. Eskilsson, and D. Bigoni. A stabilised nodal spectral element method for fully nonlinear water waves. *Journal of Computational Physics*, 318:1–21, 2016.

J.D. Fenton. The numerical solution of steady water wave problems. *Computers and Geosciences*, 14(3):357–368, 1988.

P. Ferrant and D. Le Touzé. Simulation of sloshing waves in a 3d tank based on a pseudo-spectral method. In *16th International Workshop on Water Waves and Floating Bodies*, 2001.

P. Ferrant, D. Le Touzé, and K. Pelletier. Non-linear time-domain models for irregular wave diffraction about offshore structures. *International Journal for Numerical Methods in Fluids*, 43(10-11):1257–1277, 2003.

J. B. Frandsen. Sloshing motions in excited tanks. *Journal of Computational Physics*, 196:53–87, 2004.

M. Frigo and S.G. Johnson. The design and implementation of fftw3. *Proceedings of the IEEE*, 93(2):216–231, 2005.

D. Fructus, D. Clamond, J Grue, and Ø Kristiansen. An efficient model for three-dimensional surface wave simulations: Part i: Free space problems. *Journal of Computational Physics*, 205(2):665–685, 2005.

M. Gouin, G. Ducrozet, and P. Ferrant. Development and validation of a non-linear spectral model for water waves over variable depth. *European Journal of Mechanics - B/Fluids*, 57:115–128, 2016.

A. E. Green and P. M. Naghdi. A derivation of equations for wave propagation in water of variable depth. *Journal of Fluid Mechanics*, 78(2):237–246, 1976.

S. T. Grilli, P. Guyenne, and F. Dias. A fully non-linear model for three-dimensional overturning waves over an arbitrary bottom. *International Journal for Numerical Methods in Fluids*, 35(7):829 – 867, 2001.

J. Guermond, R. Pasquetti, and B. Popov. Entropy viscosity method for nonlinear conservation laws. *Journal of Computational Physics*, 230(11):4248–4267, 2011.

P. Guyenne and D. P. Nicholls. A high-order spectral method for nonlinear water waves over moving bottom topography. *SIAM Journal on Scientific Computing*, 30(1):81–101, 2008.

J. C. Harris, E. Dombre, M. Benoit, S. T. Grilli, and K. I. Kuznetsov. Nonlinear time-domain wave-structure interaction: A parallel fast integral equation approach. *International Journal for Numerical Methods in Fluids*, 94(2):188–222, 2022.

J. S. Hesthaven and R. M. Kirby. Filtering in legendre spectral methods. *Mathematics of Computation*, 77:1425–1452, 2008.

T. B. Johannessen and C. Swan. Nonlinear transient water waves-part i. a numerical method of computation with comparisons to 2-d laboratory data. *Applied Ocean Research*, 19:293–308, 1997.

S. Kang and F. Sotiropoulos. Numerical modeling of 3d turbulent free surface flow in natural waterways. *Advances in Water Resources*, 40:23–36, 05 2012.

G. S. Karamanos and G. E. Karniadakis. A spectral vanishing viscosity method for large-eddy simulations. *Journal of Computational Physics*, 163(1):22–50, 2000.

E. V. Laitone. The second approximation to cnoidal and solitary waves. *Journal of Fluid Mechanics*, 9(3):430–444, 1960.

C. L Lin, H. Y Lee, T. H. Lee, and L. J. Weber. A level set characteristic galerkin finite element method for free surface flows. *International Journal for Numerical Methods in Fluids*, 49(5):521–547, 2005.

Z. B. Lin, L. Qian, W. Bai, Z. H. Ma, H. Chen, J. G. Zhou, and H. B. Gu. A finite volume based fully nonlinear potential flow model for water wave problems. *Applied Ocean Research*, 106:102445, 2021.

Y. M. Liu and D. K. P. Yue. On generalized bragg scattering of surface waves by bottom ripples. *Journal of Fluid Mechanics*, 356:297–326, 1998.

M. S. Longuet-Higgins and E. D. Cokelet. The deformation of steep surface waves on water - i. a numerical method of computation. *Proceedings of the Royal Society of London. A. Mathematical and Physical Sciences*, 350(1660):1–26, 1976.

Q. W. Ma and S. Yan. Quasi ale finite element method for nonlinear water waves. *Journal of Computational Physics*, 212(1):52–72, 2006.

P. A. Madsen, R. Murray, and O. R. Sørensen. A new form of the boussinesq equations with improved linear dispersion characteristics. *Coastal Engineering*, 15(4):371–388, 1991.

M. Nazarov and J. Hoffman. Residual-based artificial viscosity for simulation of turbulent compressible flow using adaptive finite element methods. *International Journal for Numerical Methods in Fluids*, 71(3):339–357, 2013.

D. Z. Ning and B. Teng. Numerical simulation of fully nonlinear irregular wave tank in three dimension. *International Journal for Numerical Methods in Fluids*, 53(12):1847–1862, 2007.

T. Okamoto and M. Kawahara. Two-dimensional sloshing analysis by lagrangian finite element method. *International Journal for Numerical Methods in Fluids*, 11(5):453–477, 1990.

D. H. Peregrine. Long waves on a beach. *Journal of Fluid Mechanics*, 27(4):815–827, 1967.

C. Raoult, M. Benoit, and M. L. Yates. Development and validation of a 3d rbf-spectral model for coastal wave simulation. *Journal of Computational Physics*, 378:278–302, 2019.

L. Schwander, D. Ray, and J. S. Hesthaven. Controlling oscillations in spectral methods by local artificial viscosity governed by neural networks. *Journal of Computational Physics*, 431:110144, 2021.

Y. L. Shao and O. M. Faltinsen. A harmonic polynomial cell (hpc) method for 3d laplace equation with application in marine hydrodynamics. *Journal of Computational Physics*, 274:312–332, 10 2014.

C. W. Shu and S. Osher. Efficient implementation of essentially non-oscillatory shock-capturing schemes. *Journal of Computational Physics*, 77(2):439–471, 1988.

V. Stiernstrom, L. Lundgren, M. Nazarov, and K. Mattsson. A residual-based artificial viscosity finite difference method for scalar conservation laws. *Journal of Computational Physics*, 430:110100, 2021.

E. Tadmor. Convergence of spectral methods for nonlinear conservation laws. *SIAM Journal on Numerical Analysis*, 26 (1):30–44, 1989.

B. Teng and R. Eatock Taylor. New higher-order boundary element methods for wave diffraction/radiation. *Applied Ocean Research*, 17(2):71–77, 1995.

Y. Tian and S. Sato. A numerical model on the interaction between nearshore nonlinear waves and strong currents. *Coastal Engineering Journal*, 50(4):369–395, 2008.

I. Tominec and M. Nazarov. Residual viscosity stabilized rbf-fd methods for solving nonlinear conservation laws. *Journal of Scientific Computing*, 94(1):14, 2022.

C. Tong, Y. L. Shao, F. W. Hanssen, Y. Li, B. Xie, and Z. L. Lin. Numerical analysis on the generation, propagation and interaction of solitary waves by a harmonic polynomial cell method. *Wave Motion*, 88:34–56, 2019.

W. Tsai and D. K. P. Yue. Computation of nonlinear free-surface flows. *Annual Review of Fluid Mechanics*, 28(1): 249–278, 1996.

M. S. Turnbull, A. G. L. Borthwick, and R. Eatock Taylor. Numerical wave tank based on a σ-transformed finite element inviscid flow solver. *International Journal for Numerical Methods in Fluids*, 42(6):641–663, 2003.

J. VonNeumann and R. D. Richtmyer. A Method for the Numerical Calculation of Hydrodynamic Shocks. *Journal of Applied Physics*, 21(3):232–237, 04 1950.

C. B. Vreugdenhil. *Numerical Methods for Shallow-Water Flow.* Springer Dordrecht, 1994.

G Wei and J. T. Kirby. Time-dependent numerical code for extended boussinesq equations. *Journal of Waterway, Port, Coastal, and Ocean Engineering*, 121(5):251–261, 1995.

C. J. Xu and R. Pasquetti. Stabilized spectral element computations of high reynolds number incompressible flows. *Journal of Computational Physics*, 196(2):680–704, 2004.

M. L. Yates and M. Benoit. Accuracy and efficiency of two numerical methods of solving the potential flow problem for highly nonlinear and dispersive water waves. *International Journal for Numerical Methods in Fluids*, 77(10):616–640, 2015.

W. S. Yue, C. L. Lin, and V. C. Patel. Numerical simulation of unsteady multidimensional free surface motions by level set method. *International Journal for Numerical Methods in Fluids*, 42(8):853–884, 2003.

V. E. Zakharov. Stability of periodic waves of finite amplitude on the surface of a deep fluid. *Journal of Applied Mechanics and Technical Physics*, 9(2):190–194, 1968.